Geophysical Journal International

Geophys. J. Int. (2014) **197,** 768–784
Advance Access publication 2014 February 13

doi: 10.1093/gji/ggu027

Mapping 3-D mantle electrical conductivity from space: a new 3-D inversion scheme based on analysis of matrix *Q*-responses

Christoph Püthe and Alexey Kuvshinov

Institute of Geophysics, ETH Zürich, Sonneggstrasse 5, *CH*-8092 *Zurich, Switzerland. E-mail: christoph.puethe@erdw.ethz.ch*

Accepted 2014 January 21. Received 2014 January 13; in original form 2013 October 11

SUMMARY

We present a novel 3-D frequency-domain inversion scheme to recover 3-D mantle conductivity from satellite magnetic data, for example, provided by the *Swarm* mission. The scheme is based on the inversion of a new set of electromagnetic transfer functions, which form an array that we denote as matrix *Q*-response and which relate external (inducing) and internal (induced) coefficients of the spherical harmonic expansion of the time-varying magnetic field of magnetospheric origin. This concept overcomes the problems associated with source determination inherent to recent schemes based on direct inversion of internal coefficients. Matrix *Q*-responses are estimated from time-series of external and internal coefficients with a newly elaborated multivariate analysis scheme. An inversion algorithm that deals with matrix *Q*-responses has been developed. In order to make the inversion tractable, we elaborated an adjoint approach to compute the data misfit gradient and parallelized the numerical code with respect to frequencies and elementary sources, which describe the external part of the magnetic field of magnetospheric origin. Both parts of the scheme have been verified with realistic test data. Special attention is given to the issue of correlated noise due to undescribed sources.

Key words: Geomagnetic induction; Magnetic anomalies: modelling and interpretation; Satellite magnetics.

1 INTRODUCTION

Maps of the three-dimensional (3-D) electrical conductivity of Earth's mantle provide an advanced understanding of the mantle's chemical and physical properties and reflect the connectivity of constituents such as fluids and partial melt. Global 3-D electromagnetic (EM) induction studies can thus provide complementary information to global seismic tomography, which is used to ascertain the mantle's bulk mechanical properties (e.g. Becker & Boschi 2002; Romanowicz 2003).

To date, only ground-based data from the global network of geomagnetic observatories have been used to obtain global and semi-global 3-D images of mantle conductivity (e.g. Koyama *et al.* 2006; Kelbert *et al.* 2009; Tarits & Mandea 2010; Semenov & Kuvshinov 2012). However, bearing in mind that geomagnetic observatories are sparsely and irregularly distributed with large gaps in oceanic regions and the Southern Hemisphere, reliable global images of the 3-D mantle conductivity structure can hardly be obtained at present or in the foreseeable future with the use of ground-based data alone.

In contrast to ground-based measurements, satellite-borne measurements provide an excellent spatial coverage with data of uniform quality. The *Swarm* multisatellite geomagnetic mission (Friis-Christensen *et al.* 2006) prompted the development of methodologies that can recover the 3-D conductivity structure from space. Two approaches, both based on an inversion of internal (induced) coefficients of the spherical harmonic expansion (SHE) of the magnetic potential due to signals of magnetospheric origin, were elaborated. Both the time-domain approach (Velimsky 2013) and the frequency-domain approach (Püthe & Kuvshinov 2013b) yielded promising results in model studies.

However, a 3-D inversion of internal coefficients has the inherent shortcoming that it requires a precise description of the magnetospheric source, in our case consisting of external (inducing) SHE coefficients. In reality, the source is determined with inevitable errors. This injects an uncontrolled uncertainty into the resulting 3-D mantle conductivity images.

We present the concept of an alternative 3-D inverse solution that overcomes this problem. The inversion scheme is based on a 2-D array of transfer functions, hereinafter denoted as *Q*-matrix or matrix *Q*-response. The *Q*-matrix connects (at a given frequency) external and internal SHE coefficients of the magnetic potential due to signals of magnetospheric origin (Olsen 1999). This scheme avoids complications with the actual description of the source. Only the structure of the source, namely the specific set of SHE terms that are significant for its description, needs to be known. Data analysis also allows for a direct estimation of uncertainties, which can be incorporated into the inversion scheme. Moreover, the approach permits the use of intermittent data (e.g. from different satellite missions that are separated in time).

The determination of time-series of external and internal coefficients is a pre-requisite for our formulation. The time-series will be available as *Swarm* data product, provided by the comprehensive inversion (CI, *cf.* Sabaka *et al.* 2013). The CI aims to separate contributions to the magnetic measurements from various sources (core, lithosphere, ionosphere and magnetosphere) in the form of corresponding SHE coefficients.

This paper is organized as follows. Matrix Q-responses are introduced in Section 2. They are estimated with a newly developed multivariate analysis scheme that we outline in the same section. The inversion algorithm is described in Section 3, in which we also present results of test studies. Several critical aspects of our methods and the inversion results are discussed in Section 4. A summary of the work presented in this paper and an outlook to future activities are given in Section 5.

2 ESTIMATION OF MATRIX Q-RESPONSES

This section in detail describes the multivariate data analysis algorithm that we elaborated to estimate matrix Q-responses. We start with their definition, which follows directly from the SHE of the magnetic potential.

2.1 The origin of matrix Q-responses

We formulate Maxwell's equations in frequency domain as

$$\frac{1}{\mu_0}\nabla \times \mathbf{B} = \sigma \mathbf{E} + \mathbf{j}^{\text{ext}}, \tag{1}$$

$$\nabla \times \mathbf{E} = \mathrm{i}\omega \mathbf{B}. \tag{2}$$

Here, $\mathbf{B}(r, \vartheta, \varphi)$ and $\mathbf{E}(r, \vartheta, \varphi)$ are the complex Fourier transforms of magnetic flux density and electric field, respectively, with r, ϑ and φ being distance from Earth's centre, colatitude and longitude, respectively. $\mathbf{j}^{\text{ext}}(r, \vartheta, \varphi)$ is the complex Fourier transform of an impressed source current density. $\sigma(r, \vartheta, \varphi)$ is the spatial conductivity distribution in the Earth and μ_0 is the magnetic permeability of free space. This formulation neglects displacement currents, which are irrelevant in the considered frequency range. Note that the dependence of $\mathbf{B}$, $\mathbf{E}$ and $\mathbf{j}^{\text{ext}}$ on angular frequency ω is omitted but implied. Also note that we adopted the Fourier convention

$$f(t) = \frac{1}{2\pi}\int_{-\infty}^{\infty} f(\omega)\mathrm{e}^{-\mathrm{i}\omega t}\,\mathrm{d}\omega. \tag{3}$$

In the source-free region above the conducting Earth, but below the region enclosed by the current $\mathbf{j}^{\text{ext}}$ (in our case the magnetosphere), eq. (1) reduces to $\nabla \times \mathbf{B} = 0$. $\mathbf{B}$ is thus a potential field and can be written as gradient of a scalar magnetic potential V, that is, $\mathbf{B} = -\nabla V$. Since $\mathbf{B}$ is solenoidal, V satisfies Laplace's equation ($\nabla^2 V = 0$) and can be represented as sum of external and internal parts, $V = V^{\text{ext}} + V^{\text{int}}$, which read

$$V^{\text{ext}} = a\sum_{n,m}\varepsilon_n^m(\omega)\left(\frac{r}{a}\right)^n Y_n^m(\vartheta, \varphi), \tag{4}$$

$$V^{\text{int}} = a\sum_{k,l}\iota_k^l(\omega)\left(\frac{r}{a}\right)^{-(k+1)} Y_k^l(\vartheta, \varphi). \tag{5}$$

Here, a is Earth's mean radius, $\varepsilon_n^m(\omega)$ and $\iota_k^l(\omega)$ are the SHE coefficients of the external (inducing) and internal (induced) parts of the potential and Y_n^m is the spherical harmonic of degree n and order m

$$Y_n^m(\vartheta, \varphi) = P_n^{|m|}(\cos\vartheta)\mathrm{e}^{\mathrm{i}m\varphi}, \tag{6}$$

with $P_n^{|m|}(\cos\vartheta)$ being the Schmidt quasi-normalized associated Legendre polynomial of degree n and order $|m|$. Note that we, for simplicity, use the conventions

$$\sum_{n,m} = \sum_{n=1}^{N_\varepsilon}\sum_{m=-n}^{n} \quad \text{and} \quad \sum_{k,l} = \sum_{k=1}^{N_\iota}\sum_{l=-k}^{k}, \tag{7}$$

where N_ε and N_ι are maximum (cut-off) degrees for external and internal coefficients, respectively. Also note that in eqs (4) and (5), we use different indices for external and internal coefficients to account for the 3-D conductivity structure. In a 1-D Earth (in which conductivity is only a function of depth), every external coefficient only induces one internal coefficient of the same degree and order. They are linearly related by the (scalar) Q-response, which is defined as

$$\iota_n^m(\omega) = Q_n(\omega)\varepsilon_n^m(\omega). \tag{8}$$

Note that Q_n is independent of the order m (e.g. Bailey 1969). In a 3-D Earth, however, every external coefficient ε_n^m induces a whole series of internal coefficients ι_k^l, such that we can write

$$\iota_k^l(\omega) = \sum_{n,m} Q_{kn}^{lm}(\omega)\varepsilon_n^m(\omega), \tag{9}$$

where the Q_{kn}^{lm} form a 2-D array of transfer functions we refer to as 'matrix Q-response' or 'Q-matrix'. Note that this formulation was suggested before by Olsen (1999). The diagonal elements of this matrix mostly describe the bulk conductivity and the stratification of the subsurface—in case of a layered (1-D) Earth, they are equivalent to the scalar Q-responses. The off-diagonal elements describe a transfer of energy to coefficients of different degree and order, which only occurs if the subsurface has a 3-D structure.

2.2 Multivariate data analysis

In the context of EM sounding research, usually not more than two transfer functions are estimated for a single field component. In magnetotellurics, for instance, the horizontal components of magnetic and electric fields are related to each other by a 2×2-matrix $\mathbf{Z}$, which is known as 'impedance tensor':

$$\begin{bmatrix} E_x \\ E_y \end{bmatrix} = \begin{bmatrix} Z_{xx} & Z_{xy} \\ Z_{yx} & Z_{yy} \end{bmatrix} \begin{bmatrix} B_x \\ B_y \end{bmatrix}. \tag{10}$$

This accordingly involves the determination of two transfer functions per (output) field component (e.g. Z_{xx} and Z_{xy} for E_x; for more details, the reader is referred to Chave & Jones 2012).

One of the exceptions is the methodology of Schmucker (2003a), which combines gradient sounding and geomagnetic depth sounding, and which involves the determination of five transfer functions for one (vertical) magnetic field component. In our case, N_s transfer functions need to be determined for each internal coefficient ι_k^l, where N_s is the number of SHE terms describing the (magnetospheric) source. However, bearing in mind that this source has a large-scale spatial structure, mainly described by an equatorial ring current, a moderate number of SHE terms (e.g. $N_\mathrm{s} = 9$; with $n \le 3$, $m \le 1$) seems to be adequate to describe the source. Note that, if using coefficients of all orders m, $N_\mathrm{s} = N_\varepsilon(N_\varepsilon + 2)$.

To estimate the elements of the Q-matrix, we developed a multivariate data analysis tool based on the section-averaging approach

(e.g. Olsen 1998) and iteratively reweighted least squares (e.g. Aster *et al.* 2005). In the following, we distinguish two methods to estimate the Q-matrix—the conventional (single-frequency) approach and the multifrequency approach.

2.3 Conventional approach

In the conventional (single-frequency) approach, the Q-matrix is estimated rowwise according to eq. (9) at a set of N_ω logarithmically spaced frequencies $\omega \in \Omega$, by solving the system of linear equations

$$\mathbf{I}_k^l(\omega) = \boldsymbol{\mathcal{E}}(\omega)\mathbf{Q}_k^l(\omega) + \delta\mathbf{I}_k^l(\omega). \tag{11}$$

In this system of equations, $\mathbf{I}_k^l$ is a column vector (of length N_d) containing estimates of the time spectra (for a given ω) of the internal coefficient ι_k^l obtained in N_d segments of the full time-series, hereinafter denoted as 'events'. $\boldsymbol{\mathcal{E}}$ is an $N_d \times N_s$ system matrix containing the respective estimates of the time spectra of the external coefficients ε_n^m for ω. $\mathbf{Q}_k^l$ is an unknown column vector of length N_s; its transpose constitutes the row of the Q-matrix corresponding to the internal coefficient ι_k^l for frequency ω. $\delta\mathbf{I}_k^l$ is the vector of residuals.

The length of the time segments depends on ω and in general is a small multiple of the associated period $T = 2\pi/\omega$. Short segments increase N_d, but in turn also increase the spectral leakage. We found that segment lengths of $3T - 8T$ yield best results. The time segments overlap to improve statistical efficiency and are tapered before performing the Fourier transform to decrease the spectral leakage (e.g. Chave & Jones 2012).

The standard least-squares solution of eq. (11) is

$$\hat{\mathbf{Q}}_{k,\mathrm{lsq}}^l = \left(\boldsymbol{\mathcal{E}}^\dagger\boldsymbol{\mathcal{E}}\right)^{-1}\boldsymbol{\mathcal{E}}^\dagger\mathbf{I}_k^l, \tag{12}$$

where $\hat{\mathbf{Q}}_k^l$ denotes an estimate of $\mathbf{Q}_k^l$, and superscript † stands for hermitian transpose. In order to minimize the influence of outliers on the results, eq. (11) is however solved by a robust least-squares algorithm. This algorithm consists of the repeated solution of a modified system of equations, in which a weighting matrix $\mathbf{R}$ is introduced. $\mathbf{R}$ is a diagonal matrix, containing weights based on the residuals obtained in the previous iteration. The solution of a such weighted system (in iteration j) is

$$\hat{\mathbf{Q}}_{k,\mathrm{rob}(j)}^l = \left(\boldsymbol{\mathcal{E}}^\dagger\mathbf{R}^{(j)}\boldsymbol{\mathcal{E}}\right)^{-1}\boldsymbol{\mathcal{E}}^\dagger\mathbf{R}^{(j)}\mathbf{I}_k^l. \tag{13}$$

As in the study by Schmucker (2003b), we perform three iterations, using Huber weights in the first two iterations and Tukey weights in the third iteration (e.g. Ritter *et al.* 1998). More robust schemes like repeated median estimates (e.g. Smirnov 2003) are not feasible for this multidimensional problem due to numerical limitations.

Estimating the uncertainties of transfer functions is a crucial task, especially if the latter are supposed to be used in the context of an inversion. Schmucker (2003b) pointed out that in the case of multivariate analyses with more than three unknowns, only jackknife estimates can handle bias errors due to noise in the input variables. We apply the jackknife method as it was introduced by Chave & Thomson (1989). By omitting in the robust least-squares analysis one event after the other, N_d estimates of $\mathbf{Q}_k^l$ are performed with $N_d - 1$ events each. We define $\hat{\mathbf{Q}}_k^{l(i)}$ as the leave-one-out estimate obtained by omitting the ith event and, as before, $\hat{\mathbf{Q}}_k^l$ as the estimate obtained with all events (note that each $\hat{\mathbf{Q}}_k^{l(i)}$ is estimated with the robust least-squares algorithm). We further define the pseudo-values

$$\boldsymbol{\xi}_k^{l(i)} = (N_d - N_s + 1)\hat{\mathbf{Q}}_k^l - (N_d - N_s)\hat{\mathbf{Q}}_k^{l(i)}. \tag{14}$$

The jackknife mean is just the arithmetic average of the pseudo-values, that is

$$\tilde{\mathbf{Q}}_k^l(\omega) = \frac{1}{N_d}\sum_{i=1}^{N_d}\boldsymbol{\xi}_k^{l(i)}. \tag{15}$$

The jackknife covariance matrix is finally the standard sample covariance of the pseudo-values

$$\mathbf{C}_k^l(\omega) = \frac{1}{N_d}\sum_{i=1}^{N_d}\left(\tilde{\mathbf{Q}}_k^l - \boldsymbol{\xi}_k^{l(i)}\right)\left(\tilde{\mathbf{Q}}_k^l - \boldsymbol{\xi}_k^{l(i)}\right)^\dagger. \tag{16}$$

Confidence limits for the elements of the Q-matrix are estimated from the diagonal elements of the covariance matrix $\mathbf{C}_k^l$ using t-statistics (Aster *et al.* 2005). Note that the standard estimate $\hat{\mathbf{Q}}_k^l$ and the jackknife estimate $\tilde{\mathbf{Q}}_k^l$ are usually very similar. This is also the case in our application, as tests not shown here have revealed. Thus, we can—for inversion—use the $\hat{\mathbf{Q}}_k^l$, weighted by the uncertainties computed with the jackknife analysis outlined above (*cf.* eq. 22 in Section 3.1).

2.4 Multifrequency approach

In the multifrequency approach, the system of eqs (11) is solved simultaneously for all N_ω frequencies. This in particular implies a large, sparse system matrix, which in diagonal blocks contains the $\boldsymbol{\mathcal{E}}(\omega)$ for all $\omega \in \Omega$. Solving this large system is mathematically equivalent to solving N_ω small systems (11), but computationally more expensive. The advantage of this method is the possibility to impose an additional constraint on the solution.

Bailey (1969) stated that the inverse Fourier transform of the scalar Q-response, which reflects the conductivity structure of a 1-D Earth, is a causal response function (since there cannot be an internal signal ι_n^m prior to excitation by ε_n^m). This is easily extended to a 3-D Earth, meaning that the inverse Fourier transform of each element of the Q-matrix is also a causal response function. Causal response functions are analytic and bounded function of ω everywhere in the upper half of the complex ω-plane (and in particular for real, positive ω; e.g. Landau & Lifshitz 1958). This theoretical finding coincides with the observation that response functions vary smoothly with respect to frequency (or its logarithm) for any realistic conductivity distribution.

We make use of this additional information and require each element of the Q-matrix to vary smoothly with frequency by minimizing the second derivative with respect to $\log_{10}(\omega)$. Let $\mathbf{y}$ be the vector of dependent variables (here containing the $\mathbf{I}_k^l$ of all N_ω frequencies), $\mathbf{x}$ the unknown model vector (here containing the $\mathbf{Q}_k^l$) and $\mathbf{A}$ the system matrix of explanatory variables (here containing the $\boldsymbol{\mathcal{E}}$ in diagonal blocks). The system of equations reads $\mathbf{y} = \mathbf{A}\mathbf{x} + \delta\mathbf{y}$, with $\delta\mathbf{y}$ being the vector of residuals, and its least-squares solution is

$$\hat{\mathbf{x}}_{\mathrm{lsq}} = \left(\mathbf{A}^\dagger\mathbf{A}\right)^{-1}\mathbf{A}^\dagger\mathbf{y}. \tag{17}$$

We define a regularization matrix $\mathbf{L}$ that, in our case, connects the $\mathcal{Q}_{kn}^{lm}$ of different frequencies ω and minimizes their second derivatives with respect to $\log_{10}(\omega)$. We also define a regularization parameter $\lambda > 0$ and then write the solution of the regularized least-squares problem (e.g. Aster *et al.* 2005) as

$$\hat{\mathbf{x}}_{\mathrm{reg}} = \left(\mathbf{A}^\dagger\mathbf{A} + \lambda\mathbf{L}^\top\mathbf{L}\right)^{-1}\mathbf{A}^\dagger\mathbf{y}. \tag{18}$$

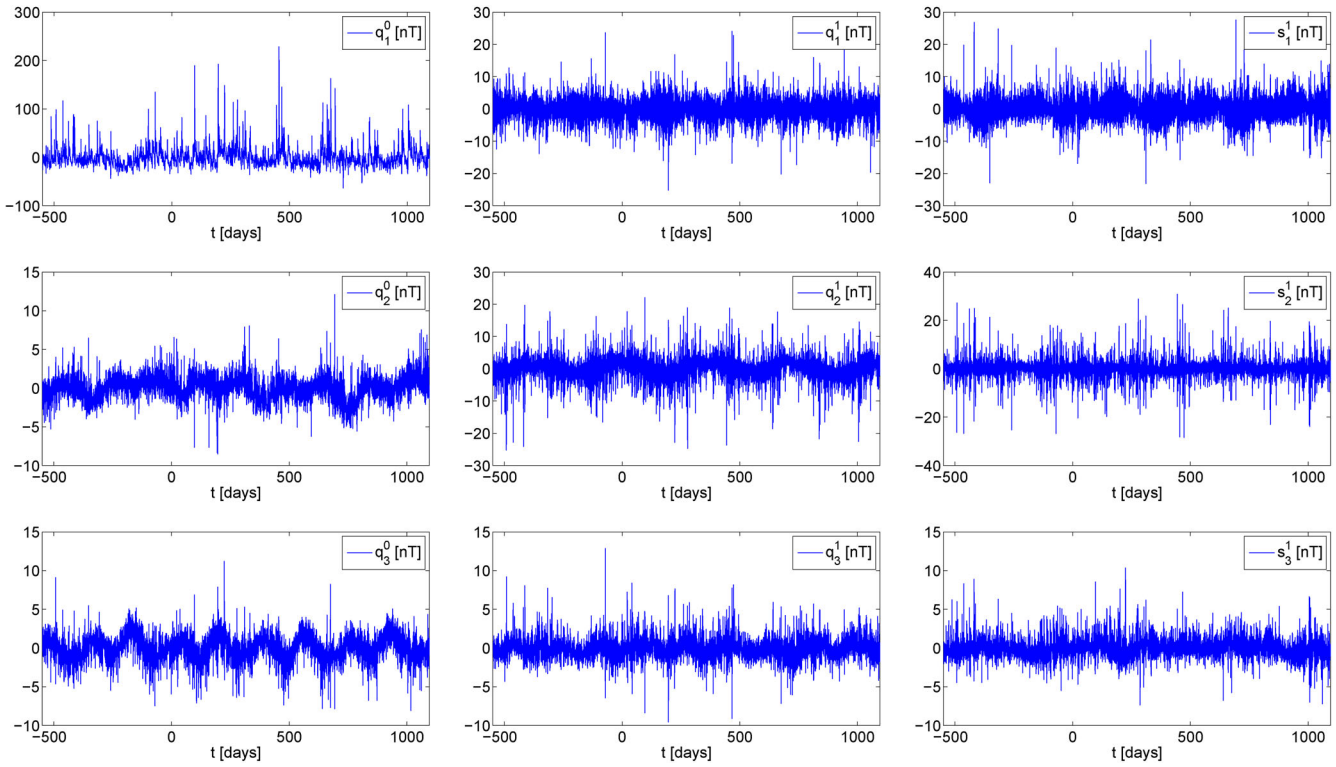

Figure 1. Time-series of the external coefficients q_n^m, s_n^m (in nT) that describe the source in our model study. The time (in days) is relative to 2000 January 1. Note that the real coefficients $q_n^m(t)$, $s_n^m(t)$ shown in this figure are related to the complex coefficients $\varepsilon_n^m(t)$ in the following way (*cf.* Kuvshinov *et al.* 2006): $\varepsilon_n^m = 1/2(q_n^m - \mathrm{i}s_n^m)$ if $m > 0$, $\varepsilon_n^m = 1/2(q_n^{|m|} + \mathrm{i}s_n^{|m|})$ if $m < 0$, and $\varepsilon_n^m = q_n^m$ if $m = 0$. Also note the different scales of the individual plots.

Combining the regularization with the above-mentioned robust least-squares algorithm finally yields the estimate

$$\hat{\mathbf{x}}_{\mathrm{reg,rob}(j)} = \left(\mathbf{A}^\dagger \mathbf{R}^{(j)} \mathbf{A} + \lambda \mathbf{L}^\top \mathbf{L}\right)^{-1} \mathbf{A}^\dagger \mathbf{R}^{(j)} \mathbf{y}, \tag{19}$$

where $\mathbf{R}$ is again a diagonal weighting matrix, and superscript $^\top$ denotes matrix transpose. The optimum amount of smoothing (determined by the value of λ) can be found by using an L-curve approach (Hansen 1992). This approach relates a norm of the data misfit, $\psi_\mathrm{d} = (\hat{\mathbf{x}} - \mathbf{A}^\dagger \mathbf{y})^\dagger \mathbf{R} (\hat{\mathbf{x}} - \mathbf{A}^\dagger \mathbf{y})$, to a norm of the smoothness of the responses, $\psi_m = (\mathbf{L}\hat{\mathbf{x}})^\dagger (\mathbf{L}\hat{\mathbf{x}})$. The optimum solution minimizes both norms.

The uncertainties can be estimated with the jackknife method outlined above, *cf.* Section 2.3. The results however have to be analysed with care. The enforced smoothness of the solution decreases the spread of the pseudo-values, obtained by individual leave-one-out estimates. This leads to an overall decrease of the estimated uncertainties, while in turn, covariances between Q-matrix elements of different frequencies are introduced.

2.5 Generation of test data

To verify the elaborated scheme and to test its performance and robustness, we designed a synthetic, but realistic test data set, consisting of time-series of external and internal SHE coefficients. A more detailed description of this data set, which was generated in the development phase of the *Swarm* satellite mission, can be found in the paper by Olsen *et al.* (2013).

Hourly mean time-series of external coefficients in a geomagnetic dipole coordinate system (up to degree $n = 3$ and order $m = 1$) were obtained by analysis of 4.5 yr of observatory data (1998 July—2002 December), details of the derivation are given in Olsen *et al.* (2006). These time-series are depicted in Fig. 1. Time-series of internal coefficients (for $k, l \leq 15$) were obtained by simulating induction in a test (target) 3-D mantle conductivity model, using a numerical solution (Kuvshinov 2008) based on a contracting integral equation (CIE) approach (Pankratov *et al.* 1995). The procedure in large parts follows the description in Kuvshinov *et al.* (2006).

The target conductivity model is shown in Fig. 2. It consists of a thin surface shell of laterally varying conductance and a layered model, which contains different small-scale and large-scale conductivity anomalies, underneath. The shell conductance is obtained by considering contributions both from sea water and sediments; for

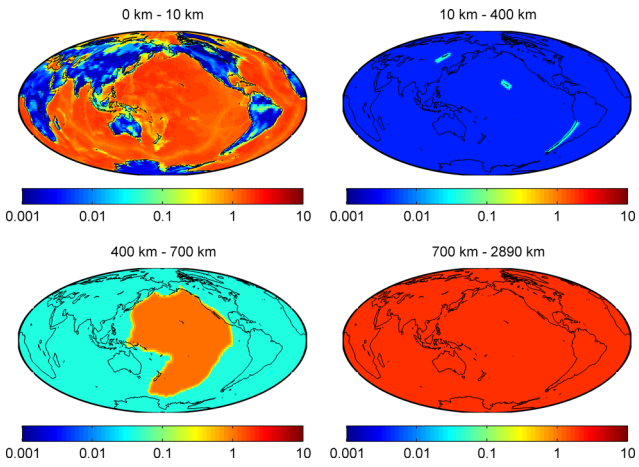

Figure 2. Target conductivity model used in our model studies, units are in S m^{-1}. Note that the conductivity of the top layer has been obtained by scaling the surface conductance map to a thickness of 10 km.

details, we refer to Manoj *et al.* (2006). The surface shell is scaled to a thickness of 10 km. Note that the same target model was used for the *Swarm* mantle conductivity studies (Püthe & Kuvshinov 2013b; Velimsky 2013).

The data obtained so far constitute a noise-free input for the multivariate analysis scheme. Estimates of the Q-matrix obtained with these noise-free data will be presented in Section 2.7.

In order to realistically simulate the full processing of *Swarm* data, we however use ε_n^m and ι_k^l to predict the magnetic field of magnetospheric origin at orbit altitudes and observatory locations (with a sampling frequency of 1 Hz). Adding the contributions due to different sources (core, lithosphere and ionosphere) yields a model of the full magnetic field at orbit altitudes and observatory locations, which is then analysed by the CI (Sabaka *et al.* 2013). The external and internal SHE coefficients of the magnetic potential due to magnetospheric sources recovered by the CI constitute a realistic test data set for the multivariate analysis scheme. We will use it in Section 2.8. Note that the CI recovers the coefficients with a sampling rate of 6 hr (ε_1^0 and ι_1^0 are recovered with a sampling rate of 1.5 hr, but resampled to 6 hr for consistency). All external coefficients used to generate the test data (up to degree $n = 3$ and order $m = 1$) are recovered. Internal coefficients are recovered up to $N_\iota = 5$. Note that the noise-free data are also resampled to 6 hr, and internal coefficients with $k > 5$ are omitted in order to have structurally similar data sets.

2.6 Some remarks on the period range

On the lower end, the period range of the matrix Q-responses is limited by the Nyquist theorem. With a sampling rate of 6 hr for the SHE coefficients (as used in the test studies presented below), the shortest period in the data is 12 hr. However, for periods up to 24 hr, the ionospheric *Sq* signals are the main cause for variations in the magnetic records. Since the CI cannot perfectly separate signals of ionospheric and magnetospheric origin, the noise level at these short periods is expected to be large. We thus only consider periods longer than 2 d.

On the upper end, the period range is limited by the length of the time-series. For a reliable least-squares analysis, the number of events must significantly exceed the number of explanatory variables (here called N_s). In our test study, we have 4.5 yr of data and $N_s = 9$. Using segments with a length of 3 T and an overlap of 50 per cent and requesting the number of events to be at least four N_s, the maximum period is of about 30 d. However, Q-responses at longer periods would be fortunate in order to resolve the conductivity structure at greater depths (see also Section 3.4).

There are two ways to acquire responses at longer periods. First, the length of the time-series scales linearly with the maximum period, thus a longer mission (or multiple separate missions) would help out. Secondly, there is obviously a trade-off between an accurate description of the source (i.e. the number of spherical harmonic terms N_s) and the maximum period of the estimated matrix Q-responses. By reducing N_s, for example, only considering induction due to sources of degree $n = 1$, we can increase the ratio without altering the number of events and thus go to longer periods. We however have to be aware that a neglected source has the effect of correlated noise, which biases the results (Egbert & Booker 1989). On the other hand, since there will be undescribed sources in real data anyway (e.g. due to field-aligned currents, *cf.* Ritter *et al.* 2013), this could be a valuable test of the robustness of the algorithm with regard to correlated noise. We will come back to this idea in a different context in Section 3.5.

2.7 Verification using noise-free test data

We now present results obtained with the test data sets described in Section 2.5. Fig. 3 shows selected elements of the Q-matrix,

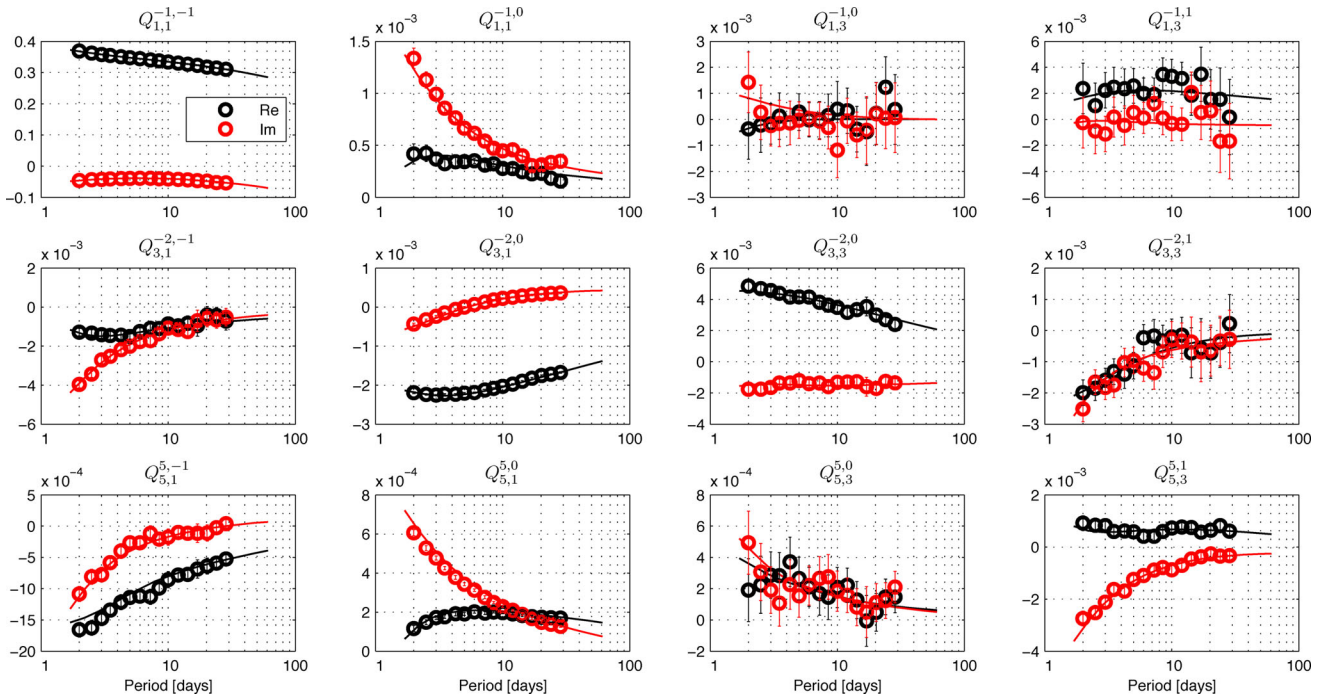

Figure 3. Selected elements of the Q-matrix, estimated from noise-free test data using the conventional approach (*cf.* Section 2.3). Rows correspond to $k = 1$, $l = -1/k = 3$, $l = -2/k = 5$, $l = 5$. Columns correspond to $n = 1$, $m = -1/n = 1$, $m = 0/n = 3$, $m = 0/n = 3$, $m = 1$. Black dots show the real part of the estimated responses, red dots the imaginary part. Solid lines correspond to theoretical predictions from the target model shown in Fig. 2.

estimated from noise-free test data using the conventional approach (*cf.* Section 2.3). Matrix Q-responses were estimated at 16 logarithmically spaced periods between 2 and 28.5 d. The estimates are compared to theoretical solutions. The latter were obtained by simulating induction due to unit amplitude spherical harmonic sources in the target model (*cf.* Fig. 2) with a CIE solver (Kuvshinov 2008).

We first note that the magnitude of the responses in the top left element is two orders higher than in the remaining elements. This is due to the fact that this is a diagonal element of the Q-matrix, that is, it describes the bulk conductivity and the 1-D structure, which dominate over the 3-D heterogeneities.

The theoretical prediction is recovered well for all elements, which verifies the performance of our multivariate analysis algorithm. The correspondence between predicted and estimated responses however differs from element to element. Weaker correspondence is, as expected, always accompanied by larger uncertainties. The predicted responses are within the confidence limits for most estimates. Good recovery is observed for the elements corresponding to the ε_1^0 source term (second column). This is due to the strong signal of ε_1^0, that is, its dominance in the data (Fig. 1). In the first row, the best resolved element however is not the one describing excitation by ε_1^0, but the diagonal element $Q_{1,1}^{-1,-1}$. This is clearly due to the fact that ι_1^{-1} is mostly excited by the corresponding external coefficient ε_1^{-1}. Note in this context that not all rows of the Q-matrix have diagonal elements if $N_\iota > N_\varepsilon$, which is the case in our study. Internal coefficients corresponding to rows without diagonal element have a much smaller magnitude, since they exclusively reflect the 3-D structure. For some features of the results—for example, the substantial difference in quality between the recovery of $Q_{5,3}^{5,0}$ and $Q_{5,3}^{5,1}$—we still do not have an obvious explanation.

Fig. 4 shows the same elements of the Q-matrix, but this time estimated using the multifrequency approach (*cf.* Section 2.4) and a regularization parameter of $\lambda = 10^5$. Note that the analysis was performed with various values of λ. Fig. 5 shows the L-curve relating ψ_d and ψ_m, that is, the norms of data misfit and smoothness of the responses. This L-curve has no distinct 'knee' in which both measures are minimized. We thus merely chose a regularization parameter for which the estimates agree well with the solution. Obviously, this approach will not be possible when analysing real data.

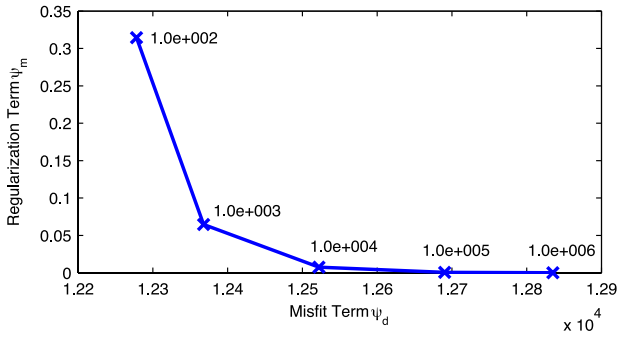

Figure 5. L-curve relating data misfit and smoothness of the responses estimated with the multifrequency approach. The values of λ are marked in the plot. The estimated responses corresponding to $\lambda = 10^5$ are shown in Fig. 4.

Due to the imposed smoothness constraint, the variation of the responses with frequency is reduced. This has no perceptible effect for the elements that were already perfectly resolved with the conventional approach, for example, $Q_{1,1}^{-1,-1}$. For most other elements, the smoothness constraint leads to a better agreement between estimates and predictions, for example, for $Q_{5,1}^{5,-1}$. When using the conventional approach, the estimates of this response function followed the general trend of the prediction, but the values at individual frequencies were offset from the solution. The smoothing constraint significantly reduces this offset, but it has two drawbacks.

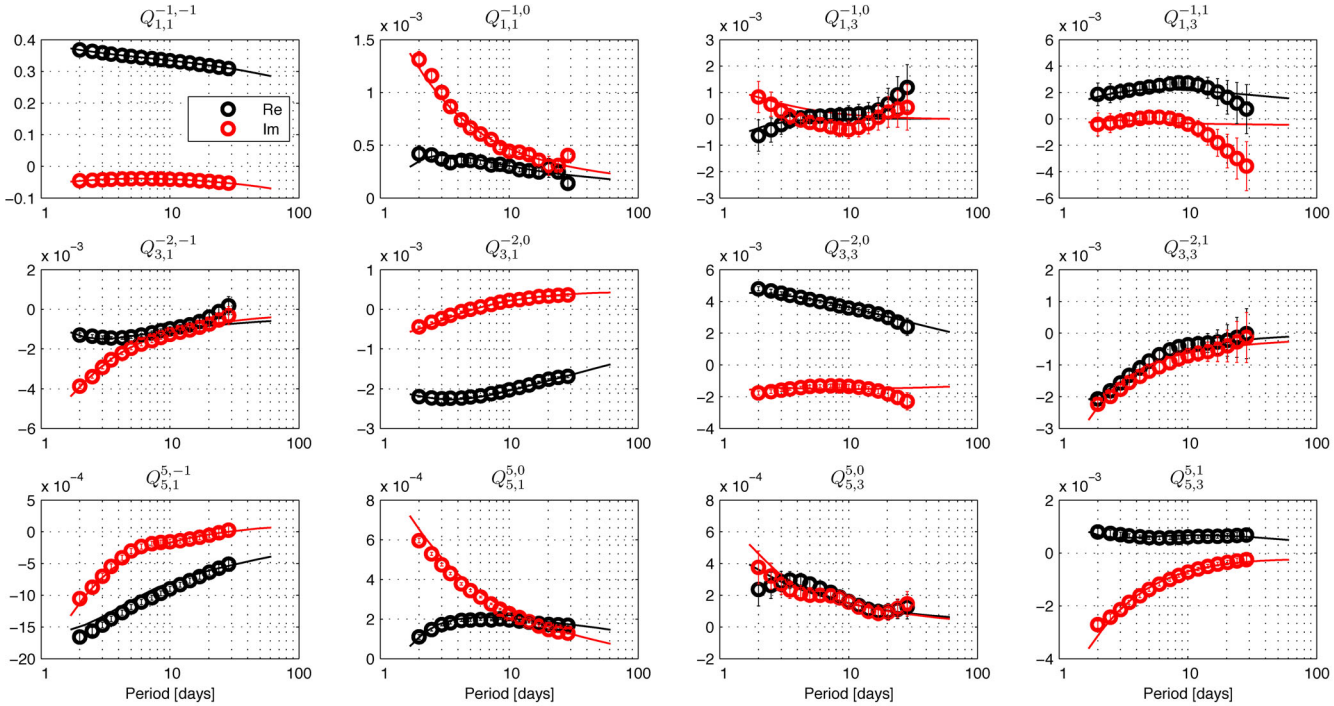

Figure 4. Selected elements of the Q-matrix, estimated from noise-free test data using the multifrequency approach (*cf.* Section 2.4). For an explanation, we refer to the caption of Fig. 3.

First, 'outlier' estimates partially lead to increased errors by 'dragging' the estimates at neighbouring frequencies away from the solution. This is, for example, the case for $Q_{1,3}^{-1,1}$. Secondly, uncertainties are generally smaller than for the conventional approach. Therefore, predictions are more often outside of the confidence limits of the estimates, even if the values are actually closer.

2.8 Verification using realistic test data

Processing results for realistic test data (i.e. test data provided by the CI, *cf.* Section 2.5) are shown in Figs 6 (conventional approach) and 7 (multifrequency approach). Let us first examine Fig. 6. As expected, the agreement between predictions and estimates is dramatically worse than for noise-free test data, and uncertainties are

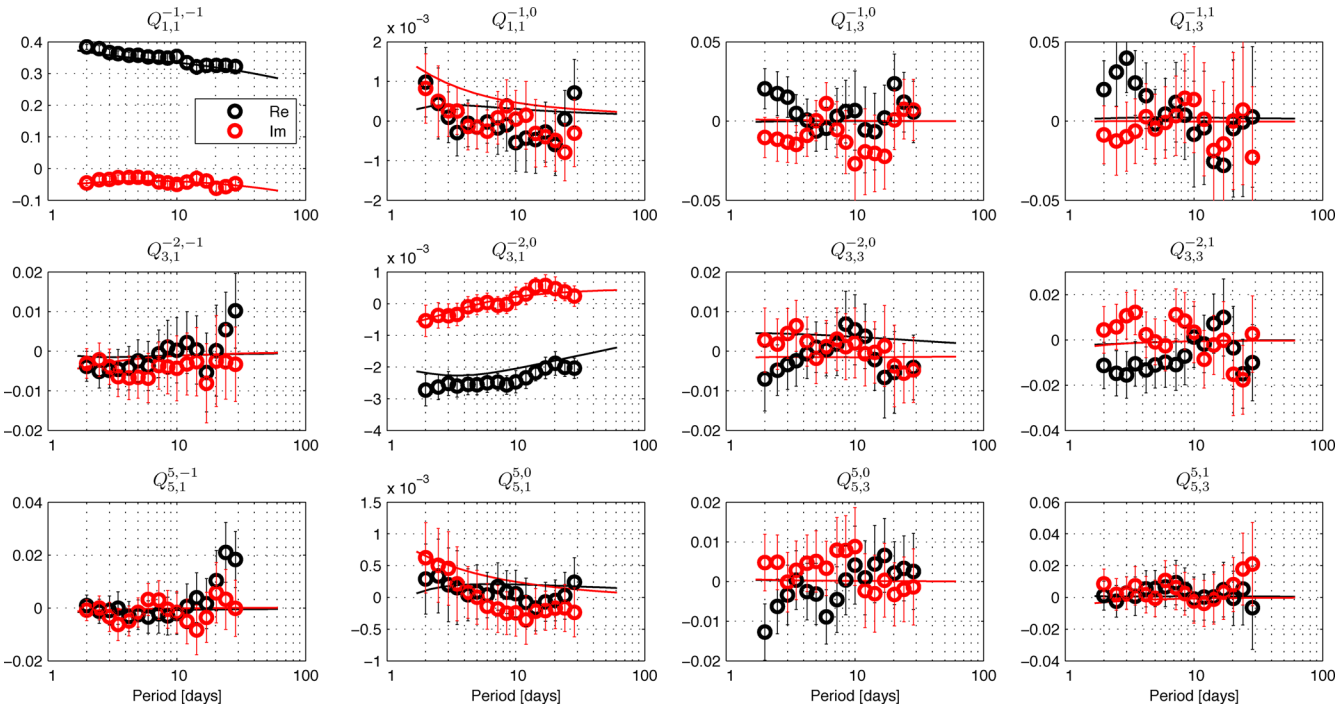

Figure 6. Selected elements of the Q-matrix, estimated from realistic test data using the conventional approach (*cf.* Section 2.3). For an explanation, we refer to the caption of Fig. 3.

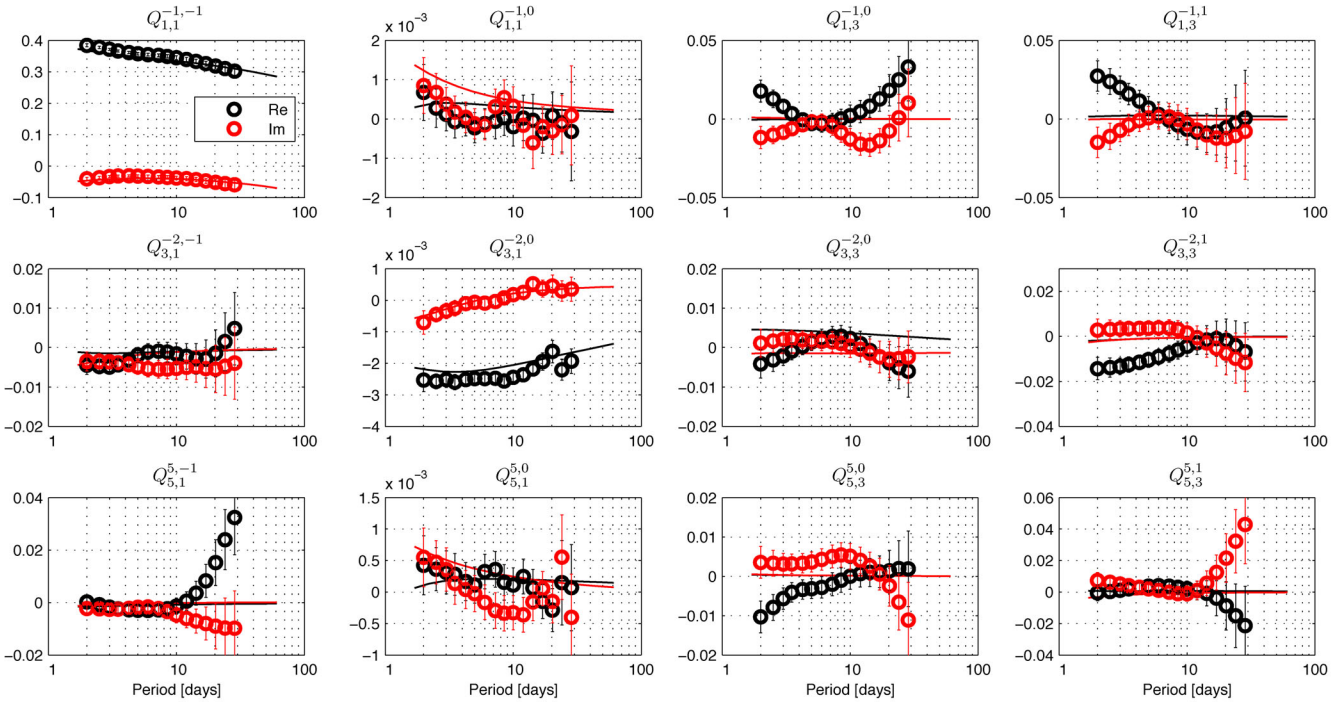

Figure 7. Selected elements of the Q-matrix, estimated from realistic test data using the multifrequency approach (*cf.* Section 2.4). For an explanation, we refer to the caption of Fig. 3.

significantly larger (but predictions are mostly within the confidence limits). In fact, most elements lack any useful information about the subsurface conductivity structure, since the magnitudes of both estimates and confidence limits are about an order larger than the corresponding predictions (e.g. $Q_{3,3}^{-2,1}$, compare with Fig. 3). Of the shown responses, only $Q_{1,1}^{-1,-1}$ (representing the 1-D structure) and $Q_{3,1}^{-2,0}$ (representing excitation by ε_1^0) are reliably resolved.

The multifrequency approach (Fig. 7) only perceptibly enhances the recovery of the (already well recovered) diagonal element $Q_{1,1}^{-1,-1}$. For most other elements, the offset between predictions and estimates is similar as in the results obtained with the conventional approach. However, uncertainties are partially dramatically reduced (e.g. for $Q_{3,3}^{-2,1}$), such that for a lot of estimates, the confidence limits do not comprise the predictions. These seemingly well-recovered responses might constitute a hazard for the inversion. Note that we again used a value of $\lambda = 10^5$, as for the noise-free data (Fig. 4).

3 3-D INVERSION OF MATRIX Q-RESPONSES

In this section, we describe how to invert matrix Q-responses for the 3-D conductivity structure of Earth's mantle. We start with the theoretical derivation (Section 3.1), thereby focusing on the adjoint approach that has been elaborated to compute the data misfit gradient (Section 3.2). After that, we give an overview of the numerical implementation (Section 3.3), investigate the resolution (Section 3.4) and verify the concept in tests with synthetic data, in that context also demonstrating the robustness of the algorithm (Section 3.5).

3.1 Concept of the 3-D inversion

We formulate the inverse problem of conductivity recovery as an optimization problem, that is, we want to minimize a penalty function $\phi(\mathbf{m}, \lambda)$ given as

$$\phi(\mathbf{m}, \lambda) = \phi_\mathrm{d}(\mathbf{m}) + \lambda \phi_m(\mathbf{m}) \tag{20}$$

with ϕ_d being the data misfit and λ and ϕ_m being a regularization parameter and a regularization term, respectively.

The data misfit $\phi_\mathrm{d}(\mathbf{m})$ is conventionally written as

$$\phi_\mathrm{d}(\mathbf{m}) = [\mathbf{F}(\mathbf{m}) - \mathbf{d}]^\dagger \mathbf{C}_\mathrm{d}^{-1} [\mathbf{F}(\mathbf{m}) - \mathbf{d}], \tag{21}$$

where $\mathbf{d}$ is the data vector, here composed of the observed (estimated) matrix Q-responses, and $\mathbf{m}$ is the model vector, composed of the N_m model parameters, which in our case describe the conductivity structure of Earth's mantle. $\mathbf{F}$ is the functional solving the forward problem, that is, predicting the matrix Q-responses for a given $\mathbf{m}$. $\mathbf{C}_\mathrm{d}$ is the data covariance matrix and assumed to be diagonal (i.e. to contain only the squared uncertainties of the elements of the Q-matrix). With this assumption, which we will justify in Section 4, we can rewrite eq. (21) in the following form:

$$\phi_\mathrm{d}(\mathbf{m}) = \sum_{\omega \in \Omega} \sum_{k,l} \sum_{n,m} \frac{\left| Q_{kn}^{lm,\mathrm{pred}}(\mathbf{m}, \omega) - Q_{kn}^{lm,\mathrm{obs}}(\omega) \right|^2}{\left(\delta Q_{kn}^{lm,\mathrm{obs}}(\omega) \right)^2}. \tag{22}$$

In this representation, $\phi_\mathrm{d}(\mathbf{m})$ is the weighted sum of the squared differences between observed and predicted (modelled) Q-matrix elements at all frequencies $\omega \in \Omega$, with the uncertainties $\delta Q_{kn}^{lm,\mathrm{obs}}(\omega)$ serving as weights.

The regularization term $\phi_m(\mathbf{m})$ is conventionally written as

$$\phi_m(\mathbf{m}) = \mathbf{m}^\top \mathbf{C}_m^{-1} \mathbf{m}, \tag{23}$$

where $\mathbf{C}_m$ is the model covariance matrix. It is often more convenient not to define $\mathbf{C}_m$, but the regularization matrix $\mathbf{W}$, such that $\mathbf{W}^\top \mathbf{W} = \mathbf{C}_m^{-1}$. With this definition, we can rewrite eq. (23) as

$$\phi_m(\mathbf{m}) = (\mathbf{W}\mathbf{m})^\top (\mathbf{W}\mathbf{m}). \tag{24}$$

$\mathbf{W}$ is supposed to smooth the solution, its form depends on the desired level of smoothness and the parametrization of the model.

Due to the non-linearity of 3-D EM inverse problems, iterative descent methods (e.g. Nocedal & Wright 2006) are typically the methods of choice. These methods require a computation of the gradient of the penalty function ϕ with respect to the model parameters, that is

$$\nabla \phi = \left(\frac{\partial \phi}{\partial m_1}, \frac{\partial \phi}{\partial m_2}, \ldots, \frac{\partial \phi}{\partial m_{N_m}} \right)^\top. \tag{25}$$

While the gradient of the regularization term is easily calculated analytically and given by

$$\nabla \phi_m(\mathbf{m}) = 2\mathbf{W}^\top \mathbf{W}\mathbf{m}, \tag{26}$$

the calculation of the data misfit gradient is more challenging. The straightforward option—brute-force numerical differentiation—requires extremely high computational loads and is approximate by nature. A much more efficient and elegant way to rigorously calculate the gradient of the misfit is provided by an adjoint approach, see, for example, Dorn *et al.* (1999). It allows the calculation of the misfit gradient for the price of only a few additional forward calculations (i.e. numerical solutions of Maxwell's equations) excited by a specific (adjoint) source. Each inverse problem setting requires the finding of explicit formulae for the adjoint source. We will now provide these formulae for our inverse problem formulation, following the general derivation by Pankratov & Kuvshinov (2010).

3.2 Adjoint approach

Let us first see how $Q_{kn}^{lm,\mathrm{pred}}$ in eq. (22) is obtained. By differentiating eqs (4) and (5) with respect to r and setting $r = a$, we obtain the radial component of the external and internal magnetic field, respectively, at Earth's surface

$$B_r^{\mathrm{ext}}(r = a, \vartheta, \varphi, \omega) = -\sum_{n,m} n \varepsilon_n^m(\omega) Y_n^m(\vartheta, \varphi), \tag{27}$$

$$\begin{aligned} B_r^{\mathrm{int}}(r = a, \vartheta, \varphi, \omega) &= \sum_{k,l} (k+1) \iota_k^l(\omega) Y_k^l(\vartheta, \varphi) \\ &= \sum_{n,m} \varepsilon_n^m(\omega) \Big[\sum_{k,l} (k+1) Q_{kn}^{lm}(\omega) Y_k^l(\vartheta, \varphi) \Big]. \end{aligned} \tag{28}$$

Note that the definition of the matrix Q-response, eq. (9), was used to derive the last equality. We can further define

$$B_{n,r}^{m,\mathrm{ext}} = -n Y_n^m(\vartheta, \varphi), \tag{29}$$

$$B_{n,r}^{m,\mathrm{int}} = \sum_{k,l} (k+1) Q_{kn}^{lm}(\omega) Y_k^l(\vartheta, \varphi) \tag{30}$$

as the radial components of the magnetic fields generated by unit amplitude spherical harmonic sources (i.e. by a source described

by $\varepsilon_n^m(\omega) = 1$). Since $B_{n,r}^{m,\text{int}} = B_{n,r}^m - B_{n,r}^{m,\text{ext}}$, we can solve these equations for the (predicted) matrix Q-responses by making use of the orthogonality of the spherical harmonics Y_k^l

$$Q_{kn}^{lm,\text{pred}} = \frac{1}{(k+1)\left\|Y_k^l\right\|^2}\int_S \left(B_{n,r}^m - B_{n,r}^{m,\text{ext}}\right) Y_k^{l*}(\vartheta,\varphi)\mathrm{d}s. \tag{31}$$

The upper asterisk * denotes complex conjugation, $\mathrm{d}s = \sin\vartheta\,\mathrm{d}\vartheta\,\mathrm{d}\varphi$, and $\left\|Y_k^l\right\|^2$ is the squared norm of the spherical harmonic Y_k^l. Note that $B_{n,r}^{m,\text{ext}}$ is independent of frequency and only describes the source geometry (as apparent from eq. 29). $B_{n,r}^m$, however, also depends on ω and Earth's conductivity structure (and thus on $\mathbf{m}$).

Taking the total derivative of the data misfit in eq. (22) yields

$$\mathrm{d}\phi_\mathrm{d}(\mathbf{m}) = 2\Re\left\{\sum_{\omega\in\Omega}\sum_{k,l}\sum_{n,m} \frac{\left(Q_{kn}^{lm,\text{pred}}(\mathbf{m},\omega) - Q_{kn}^{lm,\text{obs}}(\omega)\right)^*}{\left(\delta Q_{kn}^{lm,\text{obs}}(\omega)\right)^2}\mathrm{d}Q_{kn}^{lm,\text{pred}}(\mathbf{m},\omega)\right\}, \tag{32}$$

where $\Re$ means real part. Since $Q_{kn}^{lm,\text{pred}}$ is given by eq. (31), the only term left to derive is $\mathrm{d}Q_{kn}^{lm,\text{pred}}$. We first note that, by taking the derivative of eq. (31), we obtain

$$\mathrm{d}Q_{kn}^{lm,\text{pred}} = c_k^l\int_S \mathrm{d}B_{n,r}^m\, Y_k^{l*}(\vartheta,\varphi)\mathrm{d}s, \tag{33}$$

where we define

$$c_k^l = \frac{1}{(k+1)\left\|Y_k^l\right\|^2}. \tag{34}$$

The critical element in eq. (33) is the total derivative of the radial component of the magnetic field, $\mathrm{d}B_{n,r}^m$. To investigate this element, let us first define the operator $\mathbf{G}^{ej}(\mathbf{j}^\text{ext})$ as the 'electric field solution' of Maxwell's eqs (1)–(2) for the current source $\mathbf{j}^\text{ext}$, that is, $\mathbf{E}\equiv\mathbf{E}^\mathbf{j} = \mathbf{G}^{ej}(\mathbf{j}^\text{ext})$. Analogously, the operator $\mathbf{G}^{bj}(\mathbf{j}^\text{ext})$ represents the 'magnetic field solution' of Maxwell's eqs (1) and (2). Note that these operators are universal and do not depend on the type of code solving the forward problem.

In a similar way, we can define the operator $\mathbf{G}^{eh}(\mathbf{h}^\text{ext})$ as the electric field solution of an alternative formulation of Maxwell's equations

$$\frac{1}{\mu_0}\nabla\times\mathbf{B}^\mathbf{h} = \sigma\mathbf{E}^\mathbf{h}, \tag{35}$$

$$\nabla\times\mathbf{E}^\mathbf{h} = \mathrm{i}\omega\mathbf{B}^\mathbf{h} + \mu_0\mathbf{h}^\text{ext}, \tag{36}$$

where $\mathbf{h}^\text{ext}$ describes a distribution of magnetic dipoles. Pankratov & Kuvshinov (2010) showed that this formulation can be transformed into the more common representation of Maxwell's equations with a current source, *cf.* eqs (1) and (2). The formulation given by eqs (35) and (36) is however convenient in context of the adjoint approach, as will become clear later. An important property of the operators $\mathbf{G}^{ej}$, $\mathbf{G}^{eh}$ and $\mathbf{G}^{bj}$ are their reciprocity relations (Pankratov & Kuvshinov 2010):

$$\left\langle\mathbf{G}^{ej}(\mathbf{a}),\mathbf{b}\right\rangle = \left\langle\mathbf{a},\mathbf{G}^{ej}(\mathbf{b})\right\rangle, \tag{37}$$

$$\left\langle\mathbf{G}^{eh}(\mathbf{a}),\mathbf{b}\right\rangle = \left\langle\mathbf{a},\mathbf{G}^{bj}(\mathbf{b})\right\rangle, \tag{38}$$

where

$$\langle\mathbf{a},\mathbf{b}\rangle = \int_{\mathbf{R}^3}\mathbf{a}(\mathbf{r})\cdot\mathbf{b}(\mathbf{r})\mathrm{d}v \tag{39}$$

denotes a complex-valued bilinear scalar product. In a spherical coordinate system,

$$\langle\mathbf{a},\mathbf{b}\rangle = \int_{\mathbf{R}^3}\left(a_r b_r + a_\vartheta b_\vartheta + a_\varphi b_\varphi\right)\mathrm{d}v. \tag{40}$$

Let us now consider Maxwell's eqs (1) and (2) in an Earth's model with infinitesimally changed conductivity $\sigma + \mathrm{d}\sigma$, yielding electric and magnetic fields $\mathbf{E}+\mathrm{d}\mathbf{E}$ and $\mathbf{B}+\mathrm{d}\mathbf{B}$, respectively:

$$\frac{1}{\mu_0}\nabla\times(\mathbf{B}+\mathrm{d}\mathbf{B}) = (\sigma+\mathrm{d}\sigma)(\mathbf{E}+\mathrm{d}\mathbf{E}) + \mathbf{j}^\text{ext}, \tag{41}$$

$$\nabla\times(\mathbf{E}+\mathrm{d}\mathbf{E}) = \mathrm{i}\omega(\mathbf{B}+\mathrm{d}\mathbf{B}). \tag{42}$$

Now subtract eqs (1) and (2) from eqs (41) and (42):

$$\frac{1}{\mu_0}\nabla\times\mathrm{d}\mathbf{B} = (\sigma+\mathrm{d}\sigma)\mathrm{d}\mathbf{E} + \mathrm{d}\sigma\mathbf{E}, \tag{43}$$

$$\nabla\times\mathrm{d}\mathbf{E} = \mathrm{i}\omega\mathrm{d}\mathbf{B}. \tag{44}$$

Using the operators defined above, we can rewrite eq. (43) as

$$\frac{1}{\mu_0}\nabla\times\mathrm{d}\mathbf{B} = \sigma\mathrm{d}\mathbf{E} + \mathrm{d}\sigma\mathbf{G}^{ej}(\mathbf{j}^\text{ext}). \tag{45}$$

Note that we neglected the second-order quantity $\mathrm{d}\sigma\,\mathrm{d}\mathbf{E}$. Eqs (44) and (45) constitute a set of Maxwell's equations for the infinitesimal fields $\mathrm{d}\mathbf{E}$ and $\mathrm{d}\mathbf{B}$ excited by the 'source' $\mathrm{d}\sigma\mathbf{G}^{ej}(\mathbf{j}^\text{ext})$. Using the operator representation a second time, we obtain an expression for $\mathrm{d}\mathbf{B}$:

$$\mathrm{d}\mathbf{B} = \mathbf{G}^{bj}\left[\mathrm{d}\sigma\mathbf{G}^{ej}(\mathbf{j}^\text{ext})\right]. \tag{46}$$

So far, we did not make any assumptions about the external source current $\mathbf{j}^\text{ext}$. It has been shown (e.g. by Kuvshinov & Semenov 2012, appendix G) that for our application, $\mathbf{j}^\text{ext}$ can be considered in the form of an SHE of an equivalent sheet current. This sheet current flows in a shell at $r = b > a$ (embedded in an insulator) and produces exactly the external magnetic field $\mathbf{B}^\text{ext} = -\nabla V^\text{ext}$ at $a \le r < b$. Following the derivations in the mentioned reference and letting b approach a infinitesimally, that is, setting $b = a^+$, we can write $\mathbf{j}^\text{ext}$ as

$$\mathbf{j}^\text{ext} = \sum_{n,m}\varepsilon_n^m(\omega)\mathbf{j}_n^m, \tag{47}$$

with

$$\mathbf{j}_n^m = \frac{\delta(r-a^+)}{\mu_0}\frac{2n+1}{n+1}\mathbf{e}_r\times\nabla_\perp Y_n^m(\vartheta,\varphi). \tag{48}$$

Here, $\delta(r-a^+)$ is Dirac's delta function, $\mathbf{e}_r$ is the outward unit vector and $\nabla_\perp$ is the angular part of the gradient operator. We are interested in magnetic fields excited by elementary spherical harmonic sources $\mathbf{j}_n^m$. This yields the special case of eq. (46)

$$\mathrm{d}\mathbf{B}_n^m = \mathbf{G}^{bj}\left[\mathrm{d}\sigma\mathbf{G}^{ej}(\mathbf{j}_n^m)\right]. \tag{49}$$

Making use of reciprocity relation (38) and the definitions above, eq. (33) can be rewritten in operator form

$$\begin{aligned}\mathrm{d}Q_{kn}^{lm,\text{pred}} &= c_k^l\int_S \mathrm{d}B_{n,r}^m(r=a,\vartheta,\varphi)Y_k^{l*}(\vartheta,\varphi)\mathrm{d}s\\ &= c_k^l\int_{\mathbf{R}^3}\mathrm{d}\mathbf{B}_n^m(\mathbf{r})\mathbf{e}_r(\mathbf{r})Y_k^{l*}(\vartheta,\varphi)\delta(r-a)\mathrm{d}v\\ &= \int_{\mathbf{R}^3}\mathbf{G}^{bj}\left[\mathrm{d}\sigma\mathbf{G}^{ej}(\mathbf{j}_n^m)\right]\mathbf{h}_k^l(\mathbf{r})\mathrm{d}v\\ &= \left\langle\mathbf{G}^{eh}(\mathbf{h}_k^l),\mathrm{d}\sigma\mathbf{G}^{ej}(\mathbf{j}_n^m)\right\rangle,\end{aligned} \tag{50}$$

where

$$\mathbf{h}_k^l(\mathbf{r}) = c_k^l Y_k^{l*}(\vartheta, \varphi)\mathbf{e}_r(\mathbf{r})\delta(r-a) \tag{51}$$

is a fictitious magnetic source, consisting of radial magnetic dipoles distributed along Earth's surface with weights that are equal to $c_k^l Y_k^{l*}$.

Substituting the last line of eq. (50) into (32) yields

$$\mathrm{d}\phi_\mathrm{d}(\mathbf{m}) = 2\Re\left\{\sum_{\omega\in\Omega}\sum_{n,m}\left\langle \mathbf{G}^{eh}(\mathbf{u}_n^m), \mathrm{d}\sigma\mathbf{G}^{ej}(\mathbf{j}_n^m)\right\rangle\right\}, \tag{52}$$

with

$$\mathbf{u}_n^m = \sum_{k,l}\frac{\left(Q_{kn}^{lm,\mathrm{pred}}(\mathbf{m},\omega) - Q_{kn}^{lm,\mathrm{obs}}(\omega)\right)^*}{\left(\delta Q_{kn}^{lm,\mathrm{obs}}(\omega)\right)^2}\mathbf{h}_k^l. \tag{53}$$

With the definition of the bilinear scalar product (40), we can use eq. (52) to obtain the elements of the data misfit gradient

$$\frac{\partial\phi_\mathrm{d}}{\partial m_i} = 2\Re\left\{\sum_{\omega\in\Omega}\sum_{n,m}\int_{V_j}\left(E_r^{\mathbf{u}_n^m}E_r^{\mathbf{j}_n^m} + E_\vartheta^{\mathbf{u}_n^m}E_\vartheta^{\mathbf{j}_n^m} + E_\varphi^{\mathbf{u}_n^m}E_\varphi^{\mathbf{j}_n^m}\right)\mathrm{d}v\right\}\frac{\partial\sigma_j}{\partial m_i}, \tag{54}$$

where $\mathbf{E}^{\mathbf{u}_n^m} = \mathbf{G}^{eh}(\mathbf{u}_n^m)$. This representation implies a model built from elementary volume cells V_j each having a piecewise constant conductivity σ_j. The last term in eq. (54), $\partial\sigma_j/\partial m_i$, depends on the model parametrization (*cf.* Pankratov & Kuvshinov 2010); note that the Einstein summation convention is implied for j. If the model parameters directly represent the conductivities of each cell, that is, $m_i = \sigma_i$, then $\partial\sigma_j/\partial m_i = \delta_{ij}$, where δ_{ij} is Kronecker's delta. Eq. (54) demonstrates the essence of the adjoint approach: in order to calculate the gradient of the data misfit, only one (per frequency and elementary source) additional forward modelling with excitation by the adjoint source $\mathbf{u}_n^m$ is required.

3.3 Numerical implementation

The derivations we presented so far neither depend on the choice of the forward solver [which solves Maxwell's eqs (1) and (2) for a given conductivity model and a given source] nor on the optimization method used to solve the inverse problem. In this section, we describe how we numerically implemented the concept outlined in the previous sections for the model studies presented in Section 3.5.

For forward computations, the 3-D conductivity structure σ is discretized on a regular spherical grid, consisting of $n_r \times n_\vartheta \times n_\varphi$ cells. The conductivity within each elementary volume cell is constant, thus satisfying the condition imposed by eq. (54). In order to predict electric and magnetic fields generated both by current sources $\mathbf{j}_n^m$ and by adjoint sources $\mathbf{u}_n^m$, we use a CIE approach (extensively described by Kuvshinov & Semenov 2012).

The most expensive part of the forward solution in terms of computational cost is the calculation of Green's tensors. However, the Green's tensors are actually independent of the 3-D model (Kuvshinov & Semenov 2012). To make the inversion algorithm more efficient, we thus isolated their computation from the rest of the forward calculations, such that it does not need to be repeated in each iteration of the inversion scheme. A parallelization with respect to N_ω frequencies and to N_s elementary sources $\mathbf{j}_n^m$ has been implemented for a further acceleration of the calculations.

The inversion domain is divided into N_r layers of possibly variable thicknesses, which do not necessarily coincide with the n_r layers used for forward modelling. Since our data are transfer functions relating SHE coefficients of the magnetic potential, it is most natural to also parametrize the model domain in terms of spherical harmonics, as it has been done previously by, for example, Kelbert *et al.* (2008). Within each layer, conductivity is thus defined as a finite sum of spherical harmonics up to a cut-off degree L, that is, the number of model parameters N_m is given by $N_m = N_r(L+1)^2$. For derivations and a more thorough description of this parametrization, the reader is referred to Püthe & Kuvshinov (2013b). Note that our modular inversion code also offers the option to parametrize the inversion domain with volume cells of constant conductivity (i.e. like the forward domain).

The regularization matrix $\mathbf{W}$ introduced in Section 3.1 serves as smoothing operator. Radial smoothing, that is, regularization across layer boundaries, is applied by a finite difference approximation of the vertical gradient (acting on the respective spherical harmonic coefficients). Within each layer, lateral smoothing consists of down-weighting spherical harmonics of higher degrees. Note that this regularization scheme is similar to the scheme previously presented by Kelbert *et al.* (2008), who however defined the inverse of $\mathbf{W}$.

To minimize the penalty function given in eq. (20), our modular inversion code offers the option to choose between several popular optimization methods—non-linear conjugate gradients, quasi-Newton and limited-memory quasi-Newton (LMQN). Tests not shown here have revealed that the LMQN method is superior to the other options in terms of accuracy versus computational cost, we thus apply it in this study. Our implementation of the method follows Nocedal & Wright (2006). The iterative formula for updating the model vector $\mathbf{m}$ is

$$\mathbf{m}^{(k+1)} = \mathbf{m}^{(k)} - \alpha^{(k)}\mathbf{H}^{(k)}(\nabla\phi)^{(k)}, \tag{55}$$

where $\mathbf{H}^{(k)}$ is an approximation to the inverse Hessian matrix, updated at every iteration k, using the limited-memory Broyden–Fletcher–Goldfarb–Shanno formula (e.g. Nocedal & Wright 2006). The step length $\alpha^{(k)}$ is computed by an inexact line search and chosen to satisfy the Wolfe conditions (Nocedal & Wright 2006).

We start each inversion with strong regularization. After convergence, the value of the regularization parameter λ is decreased, and the results obtained with the previous λ are used as starting model. This gradual adaptation of the amount of regularization constrains the solution to be close to the global minimum in every stage of the iterative inversion. The final result is picked from a trade-off curve (L-curve, *cf.* Hansen 1992) that relates data misfit ϕ_d and regularization term ϕ_m for the runs with different λ.

3.4 Resolution studies

This section is dedicated to testing the performance of the inversion algorithm and investigating the resolution that can be achieved with ideal data at depths between 10 and 1600 km (note that very similar resolution studies were performed by Kelbert *et al.* 2008; Koch & Kuvshinov 2013). To this purpose, we generated eight different synthetic data sets, each of them consisting of matrix Q-responses (for $n \le 3$, $m \le 1$, $k, l \le 15$) at 11 logarithmically spaced periods between 2 and 30 d. These responses were computed by simulating induction in eight different conductivity models, differing in the depth of a laterally heterogeneous layer, which is embedded in a realistic 1-D background structure (Fig. 8). The depth ranges of this anomalous layer are 10–100, 100–250, 250–410, 410–520, 520–670, 670–900, 900–1200 and 1200–1600 km, respectively. The heterogeneous layer has a checkerboard-like conductivity structure,

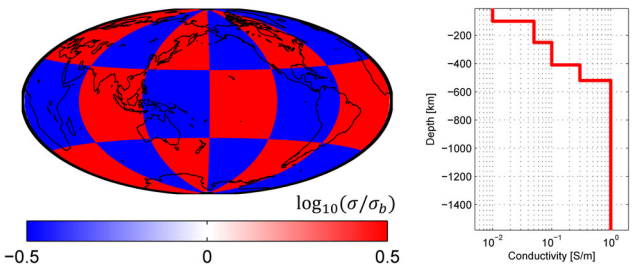

Figure 8. Left-hand side: Reference checkerboard conductivity structure of the anomalous layer used in the resolution studies. Conductivity is described as $\log_{10}(\sigma/\sigma_b)$, where σ_b is the background conductivity of the respective layer. Right-hand side: 1-D background conductivity structure σ_b in the top 1600 km.

with minimum and maximum conductivities of $\sigma_b/\sqrt{10}$ and $\sigma_b\sqrt{10}$, respectively, where σ_b denotes the background conductivity of the respective layer. The surface conductance map (*cf.* Fig. 2) comprises the top 10 km.

Each data set is now separately inverted in order to recover the heterogeneous layer at the respective depth. The inversion is initiated with the background 1-D model. The inversion domain is stratified into the eight layers described above, and the conductivity structure of each layer is described by spherical harmonics up to degree $L = 15$. Note that higher cut-off degrees do not increase the resolution, since there is no information on more detailed structures in the data. No regularization is applied. The surface conductance map is fixed during inversion. For forward modelling, each layer (including the surface shell) is discretized in 72 × 36 cells with a size of 5° × 5°.

The inversion results are presented in Fig. 9. The colouring scheme is normalized to $\log_{10}(\sigma/\sigma_b)$. Values different from zero thus indicate anomalous structures. Each column corresponds to a different inversion, that is, column n corresponds to the inversion of the nth data set, which itself corresponds to a checkerboard anomaly in the nth layer. Perfect resolution at all depths would thus be indicated by checkerboard structures in the diagonal of the 8 × 8-matrix and zeros elsewhere.

The results reveal that the 3-D mantle conductivity can—with the given data—only be recovered at depths greater than 100 km. Best resolution is achieved at depths from 500 to 900 km, but anomalous structures can be detected in the entire depth range from 100 km down to 1600 km. In all inversion runs, the conductivity structure of the laterally heterogeneous layer is smeared to the adjacent layers. This is due to the finite (and actually sparse) set of involved frequencies. The relatively poor recovery of the (comparably thin) layer extending from 410 to 520 km might be due to the same reason. Note in this context that the vertical resolution is governed by the frequency range $\omega \in \Omega$, while the lateral resolution is governed by the number of rows in the Q-matrix, that is, by the cut-off degree for internal coefficients, N_i. When using a modified data set with 14 periods between 2 and 60 d, the resolution at depths >1200 km increases (results not shown). Note that the depth resolution depends on the background conductivity structure and might thus be slightly different for real data.

3.5 Test of the inversion algorithm

In this section, we verify the performance and robustness of the inversion algorithm outlined above by recovering the target model

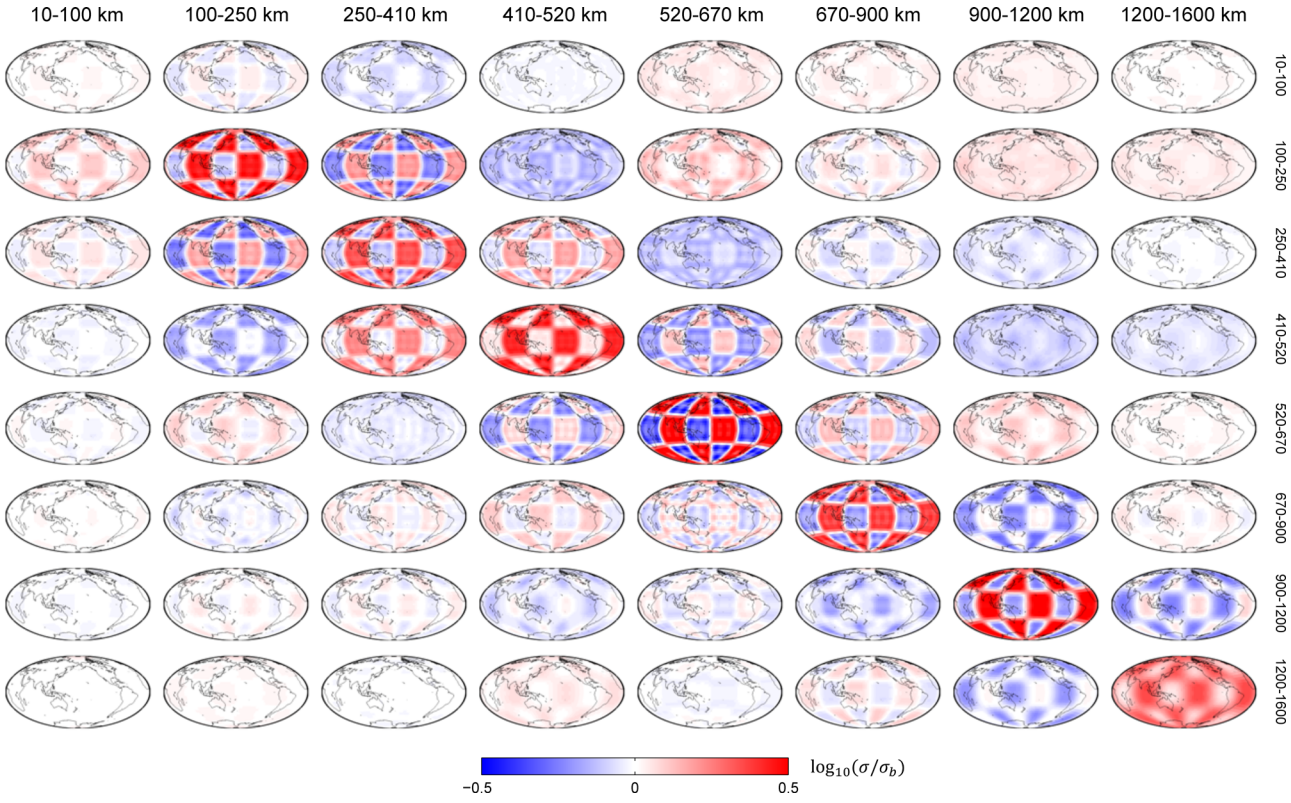

Figure 9. Results of the resolution study. Each column corresponds to an individual inversion, which tries to recover the conductivity structure of an anomalous layer buried in the depth range indicated at the top of the respective column. The depth of the resolved layers is indicated on the right. Conductivity is described as $\log_{10}(\sigma/\sigma_b)$, where σ_b is the background conductivity of the respective layer (*cf.* Fig. 8).

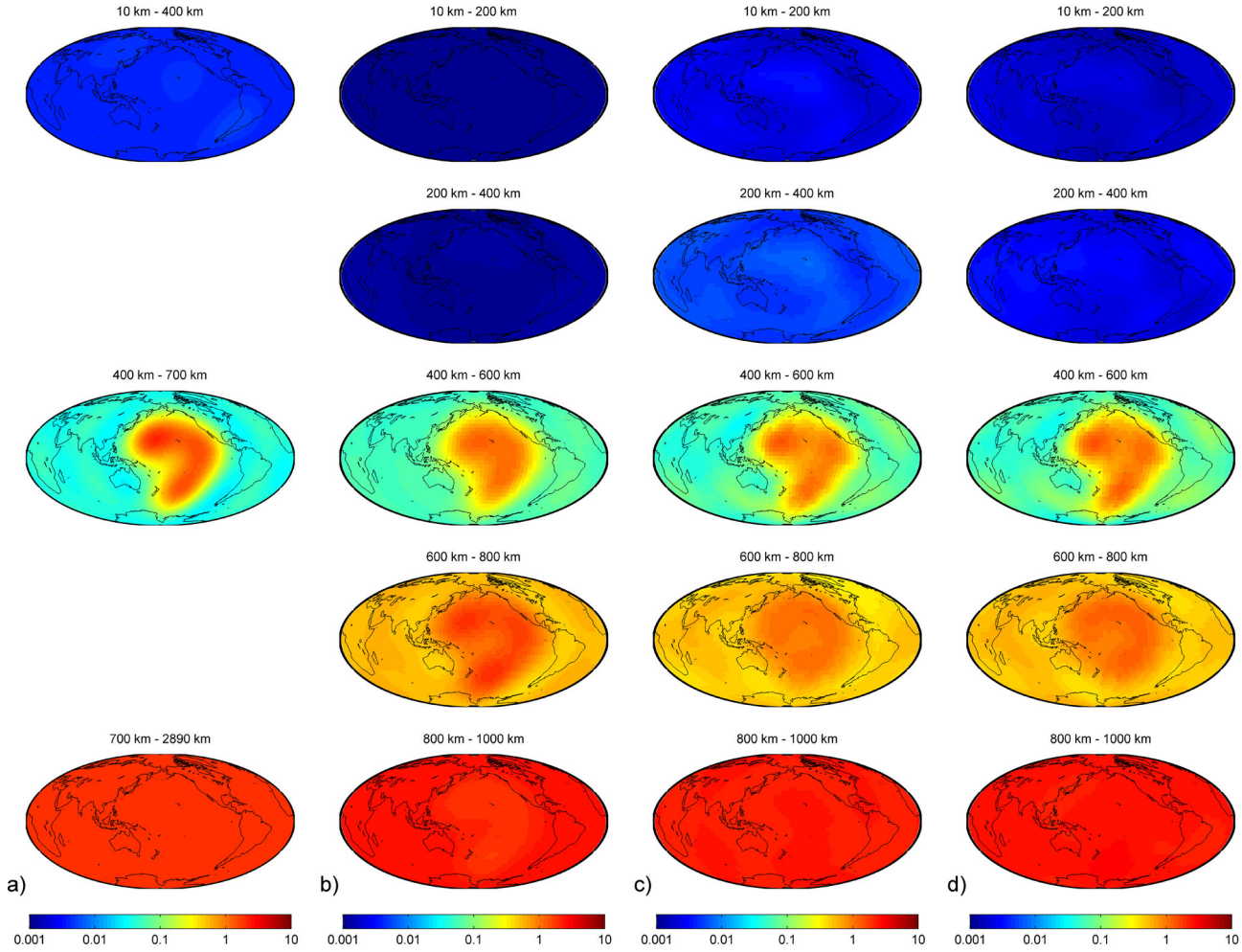

Figure 10. (a) Target conductivity model (*cf.* Fig. 2), filtered by spherical harmonics up to degree 5. Note that the surface conductance map is not shown, since it is fixed during inversion. (b) Conductivity model recovered with ideal Q-responses, that is, theoretical predictions from the target model. (c) Conductivity model recovered with Q-responses that were estimated by multivariate analysis from noise-free data with the conventional approach. (d) Conductivity model recovered with Q-responses that were estimated by multivariate analysis from noise-free data with the multifrequency approach. Units are S m^{-1}.

shown in Fig. 2, which was used to generate the test data set described in Section 2.5. As data, we will use the Q-matrices estimated with the multivariate data analysis scheme (Sections 2.7 and 2.8), shown in Figs 3–7.

We invert these data to recover the conductivity at depths between 10 and 1000 km. The surface conductance map describing the distribution of land and sea is scaled to a thickness of 10 km and fixed, that is, we do not try to recover it, as its contribution to the induced field is assumed to be known. The inversion domain consists of five layers, each having a thickness of 200 km (except for the uppermost layer, which has a thickness of 190 km). This stratification intentionally does not coincide with the stratification of the target model (*cf.* Fig. 2) in order to account for our limited knowledge of the stratification in the Earth's mantle.

For forward modelling, each layer (including the thin surface shell) is discretized in 72 $\times$ 36 cells with a size of 5° $\times$ 5°. Since our data consist of matrix Q-responses that relate SHE coefficients up to degree $k = 5$, it seems most reasonable to use a cut-off degree of $L = 5$ for the spherical harmonic representation of the conductivity in each layer. As we use an iterative solver, an initial conductivity model is required. This model consists of the laterally heterogeneous surface shell and a 1-D section underneath, which has been derived from the data by a 1-D inversion algorithm (Püthe & Kuvshinov 2013a). The conductivity at depths greater than 1000 km is fixed just like the conductivity of the surface shell.

Fig. 10 presents inversion results obtained with ideal and noise-free test data. Fig. 10(a) shows the target model 'filtered' by spherical harmonics up to degree 5, thereby representing the most detailed picture we can obtain for each layer with the implemented parametrization. Note that the small-scale anomalies in the upper mantle have disappeared, thus indicating that the resolution is limited to large-scale structures (i.e. structures of continental size).

Fig. 10(b) shows the conductivity structure recovered with ideal Q-responses, that is, the theoretical predictions that were shown as solid lines in Figs 3–7. An inversion run with such data can be considered as resolution study, which in our case is successful, since the conductivity structure is very reasonably recovered in the entire depth range.

The remaining panels of Fig. 10 show the inversion results obtained with Q-responses that were estimated by multivariate analysis from noise-free data (*cf.* Section 2.7), either using the conventional approach (Fig. 10c) or the multifrequency approach (Fig. 10d). The results show only negligible differences. In both cases, the shape of the large-scale anomaly below the Pacific is recovered very well in

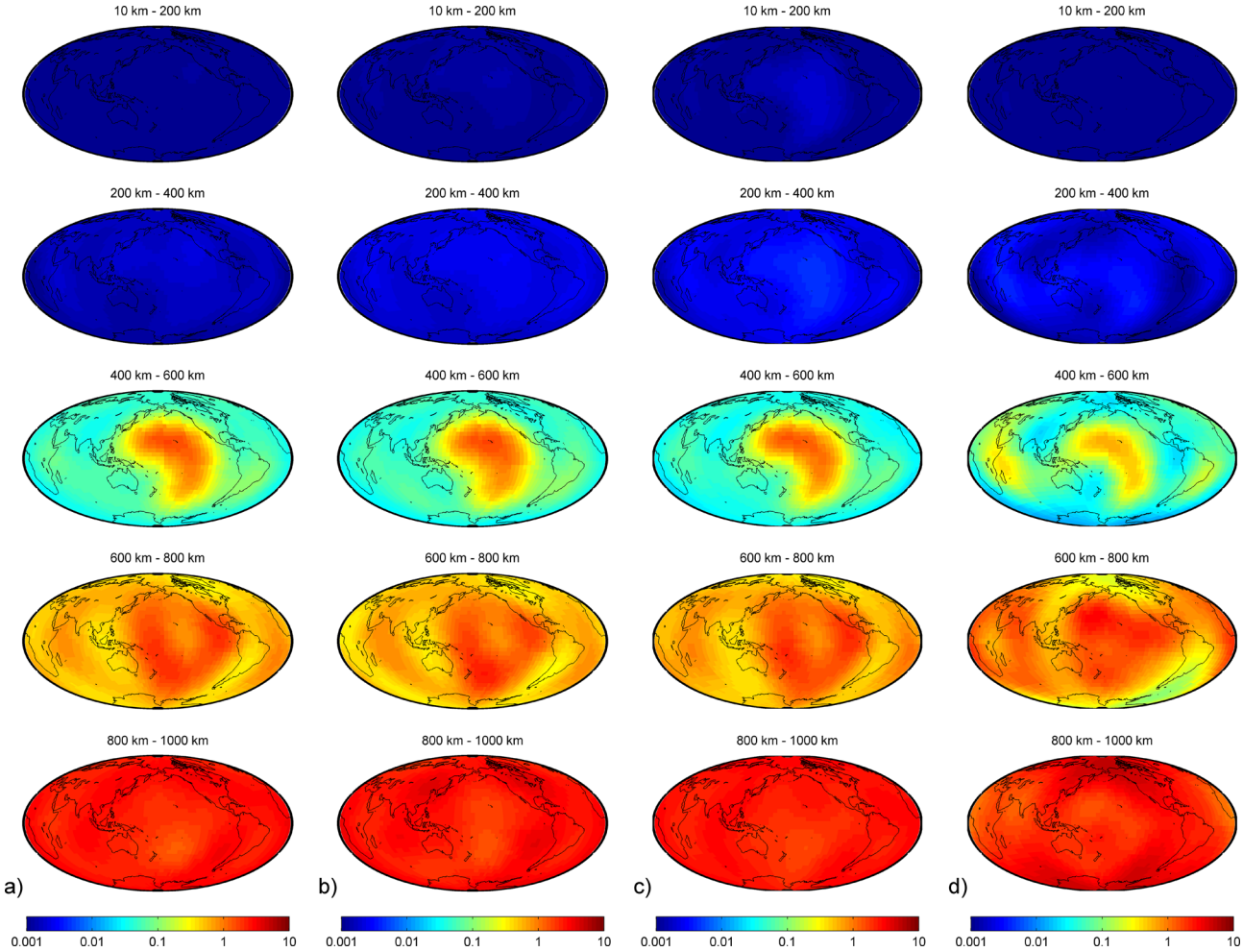

Figure 11. (a) Conductivity model recovered with Q-responses that were estimated by multivariate analysis from realistic data with the conventional approach. (b) Conductivity model recovered with Q-responses that were estimated by multivariate analysis from realistic data with the multifrequency approach. (c) Conductivity model recovered with Q-responses describing induction by the ε_1^0 source term, posterior selection. (d) Conductivity model recovered with Q-responses describing induction by the ε_1^0 source term, prior selection. Units are S m^{-1}.

the layer extending from 400 to 600 km, and conductivities of both anomaly and background match with the filtered target model. The layers extending from 10 to 200 km and from 200 to 400 km coincide almost perfectly well with the (quasi-uniform) filtered target model in this depth range. The same is true for the layer extending from 800 to 1000 km. The layer extending from 600 to 800 km samples contributions from two layers of the target model (note the different stratifications). Its conductivity distribution appears very reasonable, since the background has an intermediate conductivity when compared to both layers of the filtered target model, and the anomaly below the Pacific is clearly visible, however blurred.

Fig. 11 presents inversion results obtained with realistic data, that is, data provided by the CI (*cf.* Section 2.8). The first two panels show the results obtained by inverting Q-matrices estimated by the conventional approach and by the multifrequency approach, respectively. Again, the results are very similar and only differ in details. Compared to the results obtained by inverting noise-free data, the large conductivity anomaly below the Pacific is recovered with less details, and a few artefacts are perceptible, in particular at great depths. However, considering the partially very large uncertainties in the data (compare Figs 3 and 6), the target model is excellently recovered. These results show the robustness of our inversion algorithm.

Let us now investigate which parts of the data actually contain information about the subsurface conductivity structure, and which can be omitted without altering the inversion results. We have seen in Section 2.8 that the best-resolved elements of the Q-matrix are the diagonal terms (describing the bulk conductivity and the 1-D structure) and those referring to induction by the dominant source term, ε_1^0. It thus seems reasonable to try to recover the conductivity structure using only the column of the Q-matrix containing the terms $Q_{k,1}^{I,0}$ (visually indicated in Fig. 12a; note that, due to the chosen ordering of the coefficients, this is the second column of the Q-matrix). Note that this column contains the diagonal term $Q_{1,1}^{0,0}$ and thus the necessary information on bulk conductivity and 1-D structure.

We have to distinguish between 'prior' and 'posterior' selection of the Q-matrix elements used for inversion. By 'posterior' selection, we mean that we only use the desired column of the full Q-matrix estimated in Section 2.8. By 'prior' selection, in contrast, we mean that we estimate a new Q-matrix, this time assuming that the source is exclusively described by ε_1^0. The newly estimated Q-matrix only consists of one column, which is contaminated by correlated noise, arising from the undescribed sources of higher degree and order. Note that this also reduces the multivariate analysis to a univariate analysis.

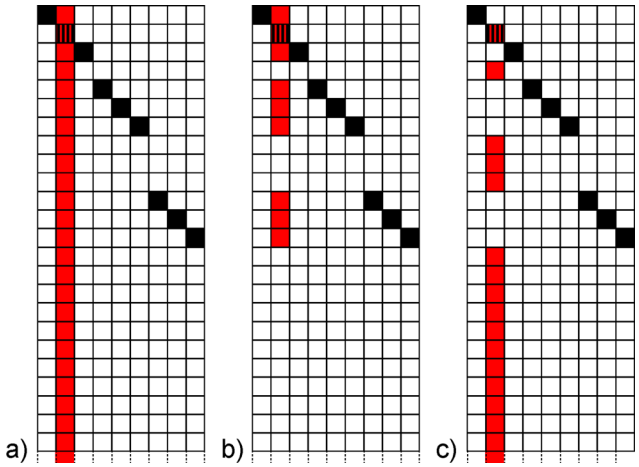

Figure 12. Sketch of the Q-matrix used in this study. Black colour marks the diagonal elements—note that not all of them are actually in the diagonal of the matrix due to the 'missing' source terms for $m > 1$. Red colour marks the elements used for different inversions. Due to the chosen ordering of the coefficients, the second column of the Q-matrix corresponds to induction by ε_1^0. (a) corresponds to the results presented in Fig. 11(c), (b) corresponds to the results presented in Fig. 13(a) and (c) corresponds to the results presented in Fig. 13(b). Note that the diagonal element of the second column is used in all three inversions.

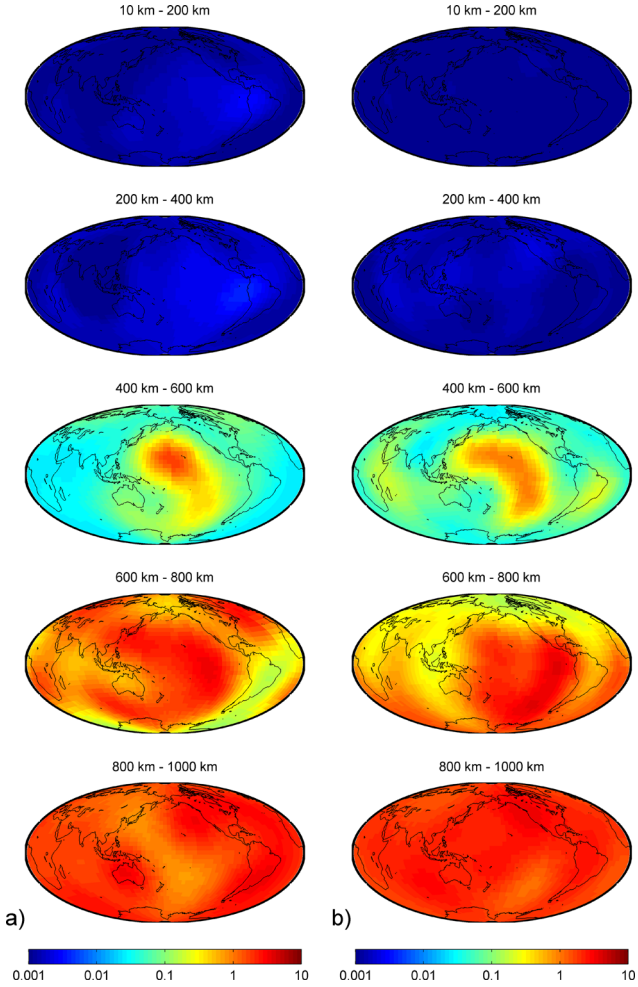

Figure 13. (a) Conductivity model recovered by inverting Q-responses describing induction by the ε_1^0 source term of Q-matrix rows with diagonal element. (b) Conductivity model recovered by inverting Q-responses describing induction by the ε_1^0 source term of Q-matrix rows without diagonal element. Units are S m^{-1}.

The results of these additional inversions are presented in the remaining panels of Fig. 11. Fig. 11(c) shows the inversion result obtained by inverting the second column of the Q-matrix estimated with the basic approach (see also Fig. 12a). The great similarity to Fig. 11(a) justifies the assumption that the information on induction due to ε_1^0 is sufficient to recover the conductivity structure. Fig. 11(d) shows the inversion result obtained by inverting the only column of a newly estimated Q-matrix, using the prior assumption that the source can be described exclusively by ε_1^0. The result clearly exhibits the effect of correlated noise. The anomaly below the Pacific is still visible, but its recovery is significantly worse than with the full data set. On top, artefacts in the solution are dramatically enhanced. This indicates the importance of the external coefficients of higher degrees and orders and shows that the source can not be described by a large-scale symmetric ring current.

A final test concerns the difference between Q-matrix elements within the same column. We have already stated in Section 2.7 that there are fundamental differences between Q-matrix rows with diagonal elements and such without diagonal elements. In the latter, ε_1^0 is typically the dominant source for the internal coefficients ι_k^l. In the former, however, the dominant source is the corresponding external coefficient of same degree and order, ε_k^l. How does this affect the inversion results? Let us return to the data set used to gain the results shown in Fig. 11(c), that is, the *a posteriori* selected column of the Q-matrix describing induction by ε_1^0, and divide it into two new data sets. The first data set contains the nine responses of rows with diagonal elements. The second data set contains the remaining 26 responses of rows without diagonal elements plus $Q_{1,1}^{0,0}$, which is needed to recover bulk conductivity and 1-D structure (Fig. 12).

The inversion results are presented in Fig. 13—panel (a) showing the results obtained by inverting responses of Q-matrix rows with diagonal element (*cf.* Fig. 12b), panel (b) those of rows without diagonal element (plus $Q_{1,1}^{0,0}$; *cf.* Fig. 12c). We can directly see that both subsets contain information about the 3-D conductivity structure, but none of them contains the full information (compare with Fig. 11c). In Q-matrix rows with diagonal elements, ε_1^0 is not the dominant source, but the signal describing induction due to ε_1^0 is above noise level (Fig. 13a—if there was no signal above noise level, we could only recover the 1-D structure). The layers extending from 400 to 600 km and from 600 to 800 km show an anomalous structure below the Pacific. Its poorly defined shape is due to the fact that we only invert Q-responses of low k and l, which describe the coarse conductivity structure. In contrast, the results in Fig. 13(b) show more details about the shape of the anomaly, but miss the coarse structure. This can be expected when inverting only Q-responses of higher degrees and orders.

Compared to the results obtained by inverting the full second column of the Q-matrix (Fig. 11c), both inversion results shown in Fig. 13 exhibit several artefacts. A closer look reveals that these artefacts are complementary to each other, that is, adding both panels of Fig. 13 will not only enhance the recovery of the conductivity anomaly below the Pacific, but also reduce the artefacts. These results indicate that we need the full column of the Q-matrix describing induction due to ε_1^0 in order to obtain reliable images of the 3-D conductivity structure in Earth's mantle.

4 DISCUSSION

4.1 Two methods to estimate the Q-matrix

To estimate the elements of the Q-matrix, we have presented two approaches. In the conventional (single-frequency) approach, responses at different frequencies are estimated individually. In the multifrequency approach, responses at all frequencies are estimated simultaneously, and they are constrained to vary smoothly with frequency, thereby satisfying some prior knowledge on transfer functions.

The multifrequency approach is an interesting tool, but it is only superior to the conventional approach in case of already relatively well-recovered transfer functions. It does not help to increase the recovery of badly resolved transfer functions, however leads to an artificial reduction of the associated uncertainties. The small uncertainties might be partially compensated by the imposed covariances between estimates at different periods. For reasons that will be discussed in the next subsection, we however cannot use these covariances in the current setup of the inversion algorithm.

As seen in Section 3.5, neither the merits nor the drawbacks of the multifrequency approach seem to have any influence on a subsequent inversion of the estimated transfer functions. We therefore decide to omit the computationally expensive multifrequency approach and recommend the conventional approach for further use.

4.2 Data weighting

In our formulation of the data misfit, we have chosen to use a diagonal data covariance matrix. This is obviously a simplification, since it neglects interrelations between different elements of the Q-matrix. Covariances between elements of different n and m are estimated together with the responses. When using the multifrequency approach, we can also determine covariances between responses at different periods. Note that the latter should be treated with care, since they are not a feature of the data, but depend on the magnitude of regularization. In contrast, our algorithm does not allow a recovery of covariances between Q-matrix elements of different k and l, since the Q-matrix is estimated row-wise. These are however a real feature of the data, because they reflect the existing interdependencies between different internal coefficients ι_k^l.

Correctly determining the full data covariance matrix is thus a very difficult task. Besides that, the use of a full matrix would prevent the application of the adjoint approach as elaborated above and hence dramatically decelerate the computations. The number of forward computations per iteration would increase by a factor $N_\iota(N_\iota + 2)$, that is, in this study by a factor 35. The computational cost would at least increase by the same factor.

These are practical arguments against the use of a full covariance matrix. We however also believe that such a dense matrix, even if it was present, would not enhance the inversion results. The data we use consist of Q-matrix elements of strongly varying quality, which is reflected by the uncertainties. By using a diagonal covariance matrix, we scale the individual responses by their uncertainties and such make sure that the influence of poorly resolved responses on the inversion results is minimized. Indeed, as we have shown, completely ignoring large parts of the data does not lead to a great change in the recovery of the conductivity model. Keeping this in mind, it might not only be unnecessary to relate different data, but even counterproductive. Relating well-resolved responses to poorly resolved responses might reduce the influence of the former on the solution and thereby lead to a degraded recovery of the conductivity structure.

In spite of our argumentation, the use of a full covariance matrix would make the analysis more self-consistent, especially if inverting matrix Q-responses estimated with the multifrequency approach. Its implementation is therefore an interesting project for the future, and its use can be expected to become less expensive with growing computational resources.

4.3 The issue of correlated noise

Correlated noise due to undescribed sources is one of the major sources of error in EM sounding research (Egbert & Booker 1989). In this section, we discuss this issue applied to matrix Q-responses.

For this study, we generated a test data set by simulating induction due to a magnetospheric source, which is described by a limited set of spherical harmonics ($N_s = 9$). The spatial structure of the source was known when the CI separated synthetic magnetic data into its constituents, represented by coefficient time-series. There is correlated noise in the recovered coefficients, for example, originating from different sampling rates (temporal leakage) and non-recovered internal/induced parts (spatial leakage). We however argue that the impact of this noise is small if compared to the impact of an undescribed (inducing) magnetospheric source. Such a source is not present in the simplified data set.

Real data will contain a larger amount of correlated noise, for example, due to field-aligned currents or magnetospheric sources of higher degree and order. In order to test the robustness of the algorithm to correlated noise, we reduced the number of sources prior to data analysis by assuming that the source can be described exclusively by its dominant term, ε_1^0. The inversion results (Fig. 11 d) revealed that a recovery of 3-D mantle conductivity anomalies is still possible, but their shape is distorted and the number of artefacts in the solution increases dramatically.

Correlated noise is hence a major issue when estimating matrix Q-responses. In this paper, we distinguished between Q-matrix rows with and without diagonal element. The Q-matrix describing the true Earth however does not have any rows without diagonal element. No matter how small a given magnetospheric source term ε_k^l might be, it will always be the dominant source for the corresponding internal coefficient ι_k^l. Neglecting existing source terms (and thereby creating Q-matrix rows without diagonal elements) will thus add large portions of correlated noise to the estimated responses in the respective rows of the Q-matrix.

When translating these findings to real data, it is apparent that we should only trust the responses of Q-matrix rows with diagonal elements, since they will be comparably unaffected by correlated noise. If the CI can—from real *Swarm* data—recover the same number of magnetospheric source terms as in this test study ($N_s = 9$), the resolution we can expect will thus rather resemble that of Fig. 13(a). A more detailed description of the source (by adding more SHE terms) might permit a better lateral resolution, but, as discussed in Section 2.6, it will limit the upper end of the period range and thus not allow the recovery of anomalous structures at great depths. A period-dependent number of source terms might be the optimum solution for this problem.

We do not know the amount of correlated noise in real data and thus can hardly estimate its effect on forthcoming inversion results. However, the analysis presented in this paper reveals that we are able to detect the correlated noise. Moreover, the Q-matrix scheme is a unique possibility to determine—already prior to

inversion—whether the data contain any reliable information on the 3-D conductivity structure and will thus be a very valuable tool when analysing the data of *Swarm* and possible further magnetic satellite missions.

5 CONCLUSIONS AND OUTLOOK

We have presented a 3-D frequency-domain inversion scheme to recover the global 3-D mantle conductivity structure using satellite magnetic data. The scheme is based on the analysis of a new 2-D array of transfer functions, named Q-matrix. The elements of the Q-matrix relate external and internal coefficients of the SHE of the magnetic potential due to magnetospheric sources. The Q-matrix is estimated by a newly developed multivariate data analysis scheme, which is based on the section-averaging approach and a robust least-squares algorithm. Uncertainties are estimated with a jackknife approach.

The inversion is made tractable by implementing a LMQN optimization method and using an adjoint approach to calculate the gradient of the penalty function. Forward computations are performed with a CIE solver. Parallelization with respect to N_ω frequencies and N_s spherical harmonic sources and an efficient implementation of the computation of Green's tensors further accelerate the calculations. The model domain is parametrized with spherical harmonics, which reflects the nature of the data.

Performance and robustness of the inversion algorithm have been tested by simulating induction due to a realistic magnetospheric source in a realistic 3-D conductivity model and recovering this model from the synthetic data. Test data provided by the CI permits an excellent recovery of 3-D structures in the mid-mantle. With periods between 2 and 30 d, 3-D structures are well resolved at depths between 100 and 1200 km; the best resolution can be expected at depths between 500 and 900 km. Lateral resolution is restricted to continental size.

Due to correlated noise, the resolution achieved in the test studies presented in this paper might not be achievable with real data. We have shown that an accurate description of the magnetospheric source is crucial for our methodology, since the resolution of the conductivity structure increases with the number of source terms considered in multivariate analysis. Describing the magnetospheric source by a large-scale symmetric ring current, represented by the SHE coefficient ε_1^0, is most probably not sufficient to map the 3-D conductivity structure of the mantle with the Q-matrix approach.

The presented tests have shown that the inversion algorithm is workable and ready to digest *Swarm* data. However, since a sufficient amount of *Swarm* data will only be available after several years, we plan to determine a preliminary 3-D mantle conductivity model with currently available data. These will include measurements of the recent single satellite missions CHAMP and Ørsted as well as data from the global network of magnetic observatories. This work will be done in cooperation with the authors of the CI (Sabaka *et al.* 2013). The results obtained with the algorithm presented above will be compared to results obtained with an algorithm analysing the data in time domain (Velimsky 2013).

The presented inversion algorithm follows a modular architecture, which does not only allow for an easy switch to different parametrizations, optimization schemes and regularization options, but also the use of different types of data, such as internal coefficient time spectra (Püthe & Kuvshinov 2013b), observatory C-responses (Semenov & Kuvshinov 2012) or time spectra of the magnetic field, determined at observatory locations (Koch & Kuvshinov 2013). Inverting further types of data (e.g. long-period impedances from observatories that are equipped with instruments measuring the electric field or voltage data from abandoned submarine telecommunication cables) is easy to implement. Developing a tool that allows a joint inversion of the different types of EM data in order to use the maximum available amount of information on global 3-D mantle conductivity is a plan for the near future.

ACKNOWLEDGEMENTS

The authors thank Nils Olsen and Takao Koyama for a careful and constructive review of the manuscript. This work has been supported by the Swiss National Science Foundation under grant No. 2000021-140711/1 and in part by the Russian Foundation for Basic Research under grant No. 12-05-00817-a.

REFERENCES

Aster, R., Borchers, B. & Thurber, C., 2005. *Parameter Estimation and Inverse Problems,* Elsevier Academic Press.

Bailey, R., 1969. Inversion of the geomagnetic induction problem, *Proc. R. Soc. Lond.,* **315,** 185–194.

Becker, T. & Boschi, L., 2002. A comparison of tomographic and geodynamic mantle models, *Geochem. Geophys. Geosyst.,* **3,** doi:10.129/2001GC000168.

Chave, A. & Jones, A., 2012. *The Magnetotelluric Method,* Cambridge Univ. Press.

Chave, A. & Thomson, D., 1989. Some comments on magnetotelluric response function estimation, *J. geophys. Res.,* **94,** 14 215–14 225.

Dorn, O., Bertete-Aquirre, H., Berryman, J.G. & Papanicolaou, G.C., 1999. A nonlinear inversion method for 3D electromagnetic imaging using adjoint fields, *Inverse problems,* **15,** 1523–1558.

Egbert, G. & Booker, J., 1989. Multivariate analysis of geomagnetic array data. 1. The response space, *J. geophys. Res.,* **94,** 14 227–14 247.

Friis-Christensen, E., Lühr, H. & Hulot, G., 2006. *Swarm*: a constellation to study the Earth's magnetic field, *Earth Planets Space,* **58,** 351–358.

Hansen, P., 1992. Analysis of discrete ill-posed problems by means of the L-curve, *SIAM Rev.,* **34,** 561–580.

Kelbert, A., Egbert, G. & Schultz, A., 2008. Non-linear conjugate gradient inversion for global EM induction: resolution studies, *Geophys. J. Int.,* **173,** 365–381.

Kelbert, A., Schultz, A. & Egbert, G., 2009. Global electromagnetic induction constraints on transition-zone water content variations, *Nature,* **460,** 1003–1007.

Koch, S. & Kuvshinov, A., 2013. Global 3-D EM inversion of Sq variations based on simultaneous source and conductivity determination: concept validation and resolution studies, *Geophys. J. Int.,* **195,** 98–116.

Koyama, T., Shimizu, H., Utada, H., Ichiki, M., Ohtani, E. & Hae, R., 2006. Water content in the mantle transition zone beneath the North Pacific derived from the electrical conductivity anomaly, in *Earth's Deep Water Cycle,* Vol. 168, pp. 171–179, eds Jacobsen, S. & van der Lee, S., AGU Geophysical Monograph Series.

Kuvshinov, A., 2008. 3-D global induction in the oceans and solid Earth: recent progress in modeling magnetic and electric fields from sources of magnetospheric, ionospheric and oceanic origin, *Surv. Geophys.,* **29,** 139–186.

Kuvshinov, A. & Semenov, A., 2012. Global 3-D imaging of mantle electrical conductivity based on inversion of observatory C-responses—I. An approach and its verification, *Geophys. J. Int.,* **189,** doi:10.1111/j.1365-246X.2011.05349.x.

Kuvshinov, A., Sabaka, T. & Olsen, N., 2006. 3-D electromagnetic induction studies using the *Swarm* constellation: mapping conductivity anomalies in the Earth's mantle, *Earth Planets Space,* **58,** 417–427.

Landau, L. & Lifshitz, E., 1958. *Statistical Physics,* Pergamon Press.

Manoj, C., Kuvshinov, A., Maus, S. & Lühr, H., 2006. Ocean circulation generated magnetic signals, *Earth Planets Space,* **58,** 429–437.

Nocedal, J. & Wright, S., 2006. *Numerical Optimization,* Springer.

Olsen, N., 1998. The electrical conductivity of the mantle beneath Europe derived from *C*-responses from 3 to 720 hr, *Geophys. J. Int.,* **133,** 298–308.

Olsen, N., 1999. Induction studies with satellite data, *Surv. Geophys.,* **20,** 309–340.

Olsen, N. *et al.*, 2006. The *Swarm* End-To-End mission simulator study: separation of the various contributions to Earth's magnetic field using synthetic data, *Earth Planets Space,* **58,** 359–370.

Olsen, N. *et al.*, 2013. The *Swarm* satellite constellation application and research facility (SCARF) and *Swarm* data products, *Earth Planets Space,* **65,** 1189–1200.

Pankratov, O. & Kuvshinov, A., 2010. General formalism for the efficient calculation of derivatives of EM frequency domain responses and derivatives of the misfit, *Geophys. J. Int.,* **181,** 229–249.

Pankratov, O., Avdeev, D. & Kuvshinov, A., 1995. Electromagnetic field scattering in a heterogeneous Earth: a solution to the forward problem, *Phys. Solid Earth,* **31,** 201–209.

Püthe, C. & Kuvshinov, A., 2013a. Determination of the 1-D distribution of electrical conductivity in Earth's mantle from *Swarm* satellite data, *Earth Planets Space,* **65,** 1233–1237.

Püthe, C. & Kuvshinov, A., 2013b. Determination of the 3-D distribution of electrical conductivity in Earth's mantle from *Swarm* satellite data: frequency domain approach based on inversion of induced coefficients, *Earth Planets Space,* **65,** 1247–1256.

Ritter, O., Junge, A. & Dawes, G., 1998. New equipment and processing for magnetotelluric remote reference observations, *Geophys. J. Int.,* **132,** 535–548.

Ritter, P., Lühr, H. & Rauberg, J., 2013. Determining field-aligned currents with the *Swarm* constellation mission, *Earth Planets Space,* **65,** 1285–1294.

Romanowicz, B., 2003. Global mantle tomography: progress status in the past 10 years, *Annu. Rev. Earth planet. Sci.,* **31,** 303–328.

Sabaka, T., Tøffner-Clausen, L. & Olsen, N., 2013. Use of the Comprehensive Inversion method for *Swarm* satellite data analysis, *Earth Planets Space,* **65,** 1201–1222.

Schmucker, U., 2003a. Horizontal spatial gradient sounding and geomagnetic depth sounding in the period range of daily variations, in *Protokoll über das 20. Kolloquium Elektromagnetische Tiefenforschung, Königstein,* pp. 228–237.

Schmucker, U., 2003b. Electromagnetic induction studies with long-periodic geomagnetic variations in Europe—I. Theory and methods of data analysis, unpublished.

Semenov, A. & Kuvshinov, A., 2012. Global 3-D imaging of mantle conductivity based on inversion of observatory *C*-responses—II. Data analysis and results., *Geophys. J. Int.,* **191,** 965–992.

Smirnov, M., 2003. Magnetotelluric data processing with a robust statistical procedure having a high breakdown point, *Geophys. J. Int.,* **152,** 1–7.

Tarits, P. & Mandea, M., 2010. The heterogeneous electrical conductivity structure of the lower mantle, *Phys. Earth planet. Inter.,* **183,** 115–125.

Velimsky, J., 2013. Determination of three-dimensional distribution of electrical conductivity in the Earth's mantle from *Swarm* satellite data: time domain approach, *Earth Planets Space,* **65,** 1239–1246.